

Three-dimensional solid particle self-assembly in thermovibrational flow: The case with unidirectional temperature gradient and concurrent vibrations

Cite as: Phys. Fluids **35**, 023323 (2023); doi: 10.1063/5.0135900

Submitted: 23 November 2022 · Accepted: 29 January 2023 ·

Published Online: 21 February 2023



View Online



Export Citation



CrossMark

Georgie Crewdson and Marcello Lappa ^{a)}

AFFILIATIONS

Department of Mechanical and Aerospace Engineering, University of Strathclyde, James Weir Building, 75 Montrose Street, Glasgow G1 1XJ, United Kingdom

^{a)} Author to whom correspondence should be addressed: marcello.lappa@strath.ac.uk

ABSTRACT

As a follow-up to earlier work [Crewdson and Lappa, “Spatial and temporal evolution of three-dimensional thermovibrational convection in a cubic cavity with various thermal boundary conditions,” Phys. Fluids **34**, 014108 (2022)], where the main focus was on the modes of convection in a three-dimensional cubic enclosure filled with a $Pr = 7$ liquid undergoing vibrations in a direction “parallel” to the imposed temperature gradient, the present study considers the modes of particle clustering, which occur when solid spheres, with density ratio $\zeta = 1.85$ or 0.3 and Stokes number (St) between 0.5 and 3.5×10^{-5} , are added to the fluid. Starting from a uniform distribution of solid particles and fluid in quiescent conditions, the governing equations for the involved phases are numerically solved in their complete, time-dependent, and non-linear form for a representative vibrational Rayleigh number (8.34×10^4), angular frequency $\Omega = 50$, and non-dimensional acceleration amplitude (γ) spanning the interval $0.4 \times 10^7 \leq \gamma \leq 3.4 \times 10^7$. It is shown that, while for relatively high values of St and/or γ , only degenerate states are obtained, where all particles collapse on planar structures, for intermediate values of such parameters, interesting (heretofore unseen) patterns are enabled. The hallmark of these phenomena is an endless squeezing and expansion of the particle formations along the direction of the temperature gradient. As confirmed by the numerical simulations, the underlying formation mechanisms rely on the combined action of the body force acting on particles due to their different densities with respect to the host fluid and the additional drag that is produced when the carrier thermovibrational flow enters a specific stage, known as “convective burst,” where the magnitude of the fluid velocity increases dramatically.

© 2023 Author(s). All article content, except where otherwise noted, is licensed under a Creative Commons Attribution (CC BY) license (<http://creativecommons.org/licenses/by/4.0/>). <https://doi.org/10.1063/5.0135900>

NOMENCLATURE

b	vibration amplitude
Nu	Nusselt number
p	pressure
P	period of vibrations
Pr	Prandtl number
Q	average particle momentum per unit mass
R	particle radius
Ra	Rayleigh number
St	Stokes number
t	time
T	temperature

u	velocity component along x
v	velocity component along y
V	velocity
w	velocity component along z
x	horizontal coordinate
y	vertical coordinate
z	spanwise coordinate

Greek Symbols

α	thermal diffusivity
β_T	thermal expansion coefficient
γ	non-dimensional acceleration amplitude

ΔT	temperature difference
ζ	particle-to-fluid density ratio
ν	kinematic viscosity
ρ	fluid density
ω	dimensional angular frequency
Ω	non-dimensional angular frequency

Subscripts

Cold	cold
Hot	hot
max	maximum
p	particle

I. INTRODUCTION

Complex fluids find a wide spectrum of versatile applications in a variety of fields, including the development of advanced granular materials, medical, bio-analytical, and microfluidic “lab-on-chip” devices, colloidal crystals, polymer solutions, metal, and organic alloys,^{1–9} just to cite a few representative cases. As all of these technological realizations require the manipulation of particles “at some stage,” finding new methods to force these to behave in certain ways or implement precise controls is therefore a subject of great importance in all these fields.

In this regard, we wish to highlight that recent progresses in *self-assembly* principles have brought about excellent prospects for tailoring certain physical (fundamental) processes and use them to define new “contactless” particle manipulation strategies by which material structure, properties, and behavior can be “programmed” on different scales with great precision.

As even a cursory review of the existing literature on this subject would immediately reveal, indeed, two alternate ways or methodological paths have been pursued to the date to meet such an objective. Namely, to induce particle self-organization, either efforts have been made to force the considered system to deliver a specific outcome through the application of artificial stimuli (such as magnetic or electric fields or coating the particles with specific substances that can turn them into self-propelling entities, see, e.g., Venema,¹⁰ Nguyen *et al.*,¹¹ and Michelin *et al.*¹²), or alternate routes have been sought/implemented to *take advantage from the inherent dynamics of these multiphase systems*, that is, practicing Mother Nature’s principles for universal behaviors.

The present study might be regarded as another example pertaining to the second line of inquiry or category of efforts, which nowadays is also known as the new field of “deterministic hydrodynamics,” namely, the utilization of innovative concepts to control distinct (solid/liquid or liquid/liquid) dispersions through the intrinsic properties of these fluid dynamic systems.^{13,14} This approach offers a vast field of exploration with plenty of open directions on numerous “facets,” which touch aspects or areas as varied as the dynamics of systems out of equilibrium, instabilities in fluid dynamic^{15–17} and order-out-of-chaos related theories. In particular, the present effort aligns with a category of studies where solid particle dynamics have been studied in conjunction with *naturally driven fluid motion*, i.e., thermal convection.

For a thorough survey on relatively recent developments in this specific field, the reader may consider, e.g., Yarin *et al.*,¹⁸ Kalilainen *et al.*,¹⁹ and Sayed *et al.*,²⁰ who examined particle motion enabled by

thermal convection driven by horizontal temperature gradients. Moreover, for the case in which gravity and the imposed temperature gradient are parallel (the so-called Rayleigh–Bénard convection, RB), it is worth citing Solomon and Gollub,^{21,22} Park *et al.*,²³ Jiang *et al.*,²⁴ and Xu *et al.*²⁵ As an example, Solomon and Gollub²¹ found particle accumulation to be passive in RB convection for the case of neutrally buoyant and very small-radius particles. On the contrary, interesting phenomena with particles accumulating along the oscillating boundaries of the fluid rolls were observed as the threshold to make RB convection time-dependent was exceeded.²² Along these lines, for the specific situation in which the flow becomes turbulent, Ref. 25, 26 could show numerically that suspended particles remain homogeneously distributed in the fluid only if their size is relatively small, whereas they tend to cluster into bands if their size is in a certain “intermediate” range (while too large particles obviously undergo sedimentation).

Even more exotic behaviors have been sought in the case where the flow is intentionally made time-dependent by replacing steady gravity with the time-varying acceleration produced by “vibrations.”^{27–34} A new category of particle attractors has been discovered accordingly, by which the dispersed solid mass tends to demix from the fluid and accumulate in specific sub-regions of the physical space having the shape of the classical “conics” curves or quadrics surfaces of projective geometry.

All these cases may be regarded as specific realizations of the overarching class of phenomena for which Haller and Sapsis³⁵ and Sapsis and Haller³⁶ could properly discern and formalize the underlying “general” principles (for which we provide here a short excursus). Such principles rest on the property of particles with finite mass and size to have a velocity that does not match exactly that of the carrier flow. Due to this difference, while the velocity of the carrier liquid obeys a divergence-free condition (which implies the fluid volume is conserved), that of particles is not bound to this mathematical restriction. As a result, no requirement for the volume occupied by a certain number of particles to be conserved exists and, accordingly, the spacing among them can vary in time while they are transported inside the fluid. It is by virtue of this simple concept that “sinks” for particles can exist in the physical space, i.e., specific loci where they can cluster (also known as “attractors” in light of the terminology coined in the more general field concerned with the dynamics of non-linear systems). For the case of thermovibrational flow, i.e., fluid motion driven by vibrations in a non-isothermal fluid, the problem is made more complex by the twofold action that vibrations can exert on the overall dynamics by influencing the fluid flow pattern and having, at the same time, a direct impact on particles due to their different densities with respect to the surrounding fluid. It is also worth noting that, by virtue of the no-volume conservation principle illustrated above, no particle-to-particle interactions are needed to support clustering and self-assembly in such cases, which therefore makes these events possible also in “dilute” dispersions. This should be regarded as a distinguishing mark with respect to the companion phenomena studied by Tabakova and Zapruanov,³⁷ Wunenburger *et al.*,³⁸ Ivanova *et al.*,³⁹ Kozlov *et al.*,⁴⁰ where inter-particle hydrodynamic effects were the main drivers for particle aggregation in vibrated liquids.

In particular, the major novelty of the present study resides in its intention to discover new particle attractors (and accordingly, to harness new particle self-assembly principles with respect to those being examined in a preexisting set of studies,^{27–34} where temperature

gradients with a significant component perpendicular to vibrations were considered. As rotating the direction of the temperature gradient with respect to the vibrations by 90° is known to change completely the properties of this type of convection in terms of stability, distribution of streamlines, and textural transitions, important modifications are also expected in terms of morphology of the loci (the aforementioned sinks) where particle accumulation can occur and the related temporal evolution of the emerging formations. In this regard, the present investigation heavily builds on the earlier (propaedeutical) study by Crewdson and Lappa,⁴¹ where particle-free thermovibrational flow was investigated for a differentially heated cubic cavity with vibrations applied in a *direction parallel to the imposed temperature gradient*. Before starting to deal with the present treatment, the reader is therefore encouraged to undertake preliminary readings of that study and become familiar with the complete characterization of the emerging time-varying convective structures provided there in terms of spatial symmetries broken or retained, topology, temporal evolution, and the sensitivity of all these aspects to the thermal boundary conditions.

II. MATHEMATICAL MODEL AND GOVERNING EQUATIONS

A. Fluid transport equations

For consistency with the aforementioned work,⁴¹ here the balance equations for mass, momentum, and energy in the fluid phase are cast in compact (dimensional) form as follows:

$$\nabla \cdot \underline{V} = 0, \tag{1}$$

$$\rho \frac{\partial \underline{V}}{\partial t} + \rho \nabla \cdot [\underline{V}\underline{V}] = -\nabla p + \mu \nabla^2 \underline{V} + \rho \underline{g}, \tag{2}$$

$$\frac{\partial T}{\partial t} + \nabla \cdot [\underline{V}T] = \alpha \nabla^2 T, \tag{3}$$

where the last term at the right-hand side of Eq. (2) accounts for the body force present in the fluid, namely, the time-periodic acceleration induced by the vibrations, which can be expressed mathematically as^{42,43}

$$\underline{g}(t) = b\omega^2 \sin(\omega t), \tag{4}$$

where ω is the angular frequency of the vibrations (rad/s) and b is the displacement of the cavity. Using the fundamental physical fluid properties appearing in these equations, some important non-dimensional parameters can be introduced, namely, the Prandtl number

$$\text{Pr} = \frac{\nu}{\alpha}, \tag{5}$$

where ν is the fluid kinematic viscosity (m^2/s) defined as ratio of the fluid dynamic viscosity μ and its density ρ , and α is the fluid thermal diffusivity (m^2/s); moreover, the Rayleigh number reads

$$\text{Ra}_\omega = \frac{b\omega^2 \beta_T \Delta T L^3}{\nu \alpha}, \tag{6}$$

where β_T is the coefficient of thermal expansion ($1/\text{K}$), ΔT is the temperature difference across the system (K), and L is the characteristic length of the cavity (m). The presence of the coefficient β_T implicitly indicates that we refer to the well-known Boussinesq approximation to account for the variations of density due to temperature inhomogeneities. This means that a linear relationship is assumed between density and

temperature in the last term at the right-hand side of Eq. (2), whereas density is considered a constant parameter in all the other terms.

Another independent influential non-dimensional number stems from the need to account for the frequency of the imposed vibrations. Yet, for consistency with Ref. 41, here we introduce it as the product of the angular frequency and the characteristic thermal diffusion time L^2/α , i.e.,

$$\Omega = \frac{\omega L^2}{\alpha}. \tag{7}$$

The non-dimensional form of the governing equations can be obtained accordingly by using reference quantities consistent with such a choice of the reference time, i.e., by scaling the length by the cavity size (L), the velocity by (α/L) , and the pressure by $(\rho\alpha^2/L^2)$. With this approach, the continuity equation remains unchanged

$$\nabla \cdot \underline{V} = 0, \tag{8}$$

while the momentum and energy equations become

$$\frac{\partial \underline{V}}{\partial t} = -\nabla p - \nabla \cdot [\underline{V}\underline{V}] + \text{Pr} \nabla^2 \underline{V} + \text{Pr} \text{Ra}_\omega T \sin(\Omega t) \hat{n}, \tag{9}$$

$$\frac{\partial T}{\partial t} + \nabla \cdot [\underline{V}T] = \nabla^2 T. \tag{10}$$

The projection of the momentum equation on the coordinate axes gives

$$\frac{\partial u}{\partial t} = -\frac{\partial p}{\partial x} - (\underline{V} \cdot \nabla \underline{V})_u + \text{Pr}(\nabla^2 \underline{V})_u, \tag{11a}$$

$$\frac{\partial v}{\partial t} = -\frac{\partial p}{\partial y} - (\underline{V} \cdot \nabla \underline{V})_v + \text{Pr}(\nabla^2 \underline{V})_v + \text{Pr} \text{Ra}_\omega T \sin(\Omega t), \tag{11b}$$

$$\frac{\partial w}{\partial t} = -\frac{\partial p}{\partial z} - (\underline{V} \cdot \nabla \underline{V})_w + \text{Pr}(\nabla^2 \underline{V})_w, \tag{11c}$$

where

$$(\underline{V} \cdot \nabla \underline{V})_u = \left(u \frac{\partial u}{\partial x} + v \frac{\partial u}{\partial y} + w \frac{\partial u}{\partial z} \right)$$

and (12a)

$$(\nabla^2 \underline{V})_u = \left(\frac{\partial^2 u}{\partial x^2} + \frac{\partial^2 u}{\partial y^2} + \frac{\partial^2 u}{\partial z^2} \right),$$

$$(\underline{V} \cdot \nabla \underline{V})_v = \left(u \frac{\partial v}{\partial x} + v \frac{\partial v}{\partial y} + w \frac{\partial v}{\partial z} \right)$$

and (12b)

$$(\nabla^2 \underline{V})_v = \left(\frac{\partial^2 v}{\partial x^2} + \frac{\partial^2 v}{\partial y^2} + \frac{\partial^2 v}{\partial z^2} \right),$$

$$(\underline{V} \cdot \nabla \underline{V})_w = \left(u \frac{\partial w}{\partial x} + v \frac{\partial w}{\partial y} + w \frac{\partial w}{\partial z} \right)$$

and (12c)

$$(\nabla^2 \underline{V})_w = \left(\frac{\partial^2 w}{\partial x^2} + \frac{\partial^2 w}{\partial y^2} + \frac{\partial^2 w}{\partial z^2} \right),$$

and u , v , and w are the fluid velocity components along x , y , and z , respectively.

B. Boundary conditions for the fluid phase

For the convenience of the reader, the system originally considered by Crewdson and Lappa⁴¹ is shown in Fig. 1. The bottom wall of the three-dimensional (3D) cubic cavity is set to $T = T_{cold}$ and the top wall to $T = T_{hot}$. The sides of the cavity are all adiabatic, all conducting, or a hybrid configuration is assumed. The vibrations are applied parallel to the temperature gradient (along the y axis).

The boundary conditions for $t > 0$ can be sketched as follows. No-slip conditions hold along all the solid walls.

For the case illustrated in Fig. 1(a), the sidewalls are adiabatic

$$\frac{\partial T}{\partial x} = 0 \text{ for } z = 0, \ z = 1, \ \text{and } t > 0, \quad (13a)$$

$$\frac{\partial T}{\partial z} = 0 \text{ for } x = 0, \ x = 1, \ \text{and } t > 0. \quad (13b)$$

For the case illustrated in Fig. 1(b), the sidewalls in the z-plane are perfectly conducting and the walls in the x-plane are adiabatic

$$\frac{\partial T}{\partial x} = 0 \text{ for } z = 0, \ z = 1, \ \text{and } t > 0, \quad (14a)$$

$$T = y \text{ for } x = 0, \ x = 1, \ \text{and } t > 0. \quad (14b)$$

For the case illustrated in Fig. 1(c), all the sidewalls are perfectly conducting, i.e.,

$$T = y \text{ for } x = 0, \ x = 1 \ \text{and } z = 0, \ z = 1 \ \text{and } t > 0. \quad (15)$$

Finally, different constant temperatures are set for all three cases at $y = 0$ and $y = 1$

$$T = 0 \text{ for } y = 0, \ 0 \leq x \leq 1, \ 0 \leq z \leq 1 \quad (16)$$

and

$$T = 1 \text{ for } y = 1, \ 0 \leq x \leq 1, \ 0 \leq z \leq 1.$$

C. Particle tracking

In line with the modus operandi successfully implemented in the companion category of studies dealing with the case of perpendicular

vibrations^{27–34} and in line with Ref. 16, here, solid particles are tracked separately in the framework of a Lagrangian approach by which the different forces acting on each particle are computed using the information provided by the numerical solution of the equations for the fluid phase, i.e., Eqs. (8)–(10). The fluid velocity field is indeed used to determine the various force terms appearing at the right-hand side of the so-called Maxey–Riley equation,⁴⁴ which in condensed form reads

$$\rho_p \frac{dV_p}{dt} = \rho \frac{DV}{Dt} + \frac{9}{2} \frac{\mu}{R_p^2} (V - V_p) + \frac{\rho}{2} \left(\frac{DV}{Dt} - \frac{dV_p}{dt} \right) + (\rho_p - \rho) b \omega^2 \sin(\omega t) \hat{n}, \quad (17)$$

where R_p , ρ_p and $V_p = [u_p, v_p, w_p]$ are the particle radius, density, and velocity, respectively. Moreover, the four terms at its right-hand side represent, respectively, the force that the undisturbed flow exerts on any solid particle, the particle drag due to its viscous interaction with the external fluid, the virtual-added mass force, and the time-varying buoyancy force resulting from the effect that the acceleration has on non-iso-dense ($\rho \neq \rho_p$) particles. The so-called Basset force is disregarded here as the considered vibration frequencies satisfy the conditions for which this force becomes negligible, see Ref. 45 and references therein. Forces due to particle interactions are also ignored as the dispersion of particles in the fluid is assumed to be dilute. The same assumption also represents the required mathematical basis by which the back influence of particles on the fluid flow can be neglected (leading to the so-called one-way approach, the reader being referred to Refs. 31 and 46 for additional reasoning about the conditions for which it can be considered applicable).

By indicating with

$$\xi = \rho_p / \rho, \quad (18)$$

the ratio of the particle to the fluid density and introducing

$$St = \frac{2 R_p^2}{9 L^2} \quad (19)$$

as the particle Stokes number, the non-dimensional form of the aforementioned Maxey–Riley equation becomes

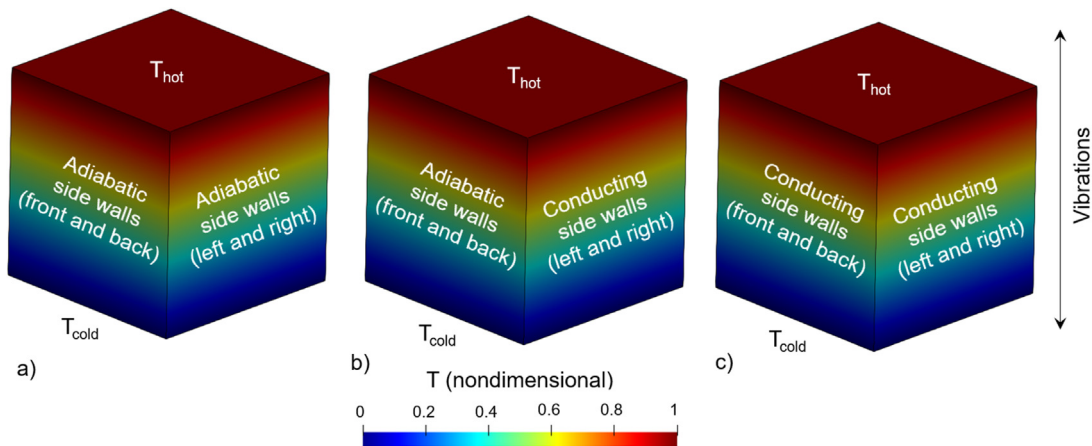


FIG. 1. Considered fluid domain and related thermal boundary conditions: (a) all sidewalls adiabatic, (b) hybrid configuration with two adiabatic and two conducting (opposing) sidewalls, (c) all sidewalls conducting.

$$\frac{dV_p}{dt} = \frac{1}{\xi + 1/2} \left[-\frac{\text{Pr}}{\text{St}} (V_p - V) + \frac{3}{2} \frac{dV}{dt} + \frac{3}{2} (V \cdot \nabla V) \right] + \frac{\xi - 1}{\xi + 1/2} \gamma \sin(\Omega t) \hat{n}, \quad (20)$$

where

$$\gamma = \frac{b\omega^2 L^3}{\alpha^2} \quad (21)$$

is the acceleration non-dimensional amplitude.

This equation has obviously to be complemented with the required treatment used to deal with particles approaching the solid walls. In the present study, these are prevented from physically penetrating the solid boundaries by making sure that the distance of their center from the wall cannot become smaller than their radius.

Particles uniformly distributed (evenly spaced) in the computational domain are considered as initial conditions at the time $t = 0$.

III. NUMERICAL METHOD

The software OpenFOAM has been employed to solve the entire set of Eulerian and Lagrangian equations with the related boundary conditions presented in Sec. II. The Maxey–Riley equation has been integrated with respect to time in the frame of a Runge–Kutta approach with linear interpolations exploited to reconstruct the fluid velocity at the positions instantaneously occupied by the particle. Detailed information about the specific schemes used in the treatments of the fluid part (the PISO i.e., the Pressure-Implicit with Splitting Operators, algorithm) is reported in the following.

A. The projection method

The set of equations (1)–(3) with the related boundary conditions [Eqs. (13)–(16)] has been solved numerically using a primitive variable technique pertaining to the general category of “projection” or “fractional step” methods. This class of techniques rests on the specific interrelation that is established in incompressible flows *between pressure and velocity*.⁴⁷ Unlike compressible flows where pressure is generally determined using the gas state equation (and therefore, it depends on density and temperature obtained by solving the continuity and energy equations, respectively), for an incompressible flow, p is only a function of another varying physical quantity, i.e., the fluid velocity V . In order to understand how this apparently innocuous observation can be used to develop an effective time-marching procedure for the determination of both p and V , it is worth starting from the simple realization that both unknowns appear in the momentum equation (which can therefore be taken as the starting point for the illustration of the methodology). In particular, this equation can be manipulated and split into sub-equations, which through combination with the incompressibility constraint lead to “new” mathematical entities not present in the original formulation, particularly suitable for the definition of a “working” algorithm. The first step along this logical process consists of neglecting the pressure term in the momentum equation

$$\frac{\partial V}{\partial t} = -\nabla \cdot [VV] + \text{Pr} \nabla^2 V + \text{Pr} Ra_\omega T \sin(\Omega t) \hat{n}, \quad (22a)$$

$$\frac{V^* - V^n}{\Delta t} = [-\nabla \cdot [VV] + \text{Pr} \nabla^2 V + \text{Pr} Ra_\omega T \sin(\Omega t) \hat{n}], \quad (22b)$$

where Δt is the time integration step. Although affected by this severe approximation, notably this equation expresses indirectly the conservation

of vorticity. Indeed, there would be no difference in the derived equation obtained by taking the curl of either Eq. (2) or Eq. (22a) because, by definition, the curl of the gradient of a function is always zero. Put differently, this means that the vorticity associated with V^* is identical to the vorticity that the effective (complete) field would possess. This observation naturally leads to introduce the next step that is the stage where V^* is made “complete” by enriching it with the previously neglected gradient of pressure, i.e.,

$$V = V^* - c \nabla p, \quad (23)$$

where c is a constant. This second step is needed on the one hand to make V^* “physical” (reintroducing the effect of the gradient of pressure) and, on the other hand, to force the final (complete) velocity to satisfy the continuity equation (not yet involved in the algorithm). This final stage is accomplished by substituting the formally corrected velocity through Eq. (23) into Eq. (1). If c is set equal to $1/\Delta t$, this operation formally closes the problem from a numerical point of view as an additional mathematical identity is obtained by which the (otherwise unknown) pressure can be obtained

$$\nabla^2 p = \frac{1}{\Delta t} \nabla \cdot V^*. \quad (24)$$

If the no-slip physical boundary conditions are used for Eq. (22), the resulting velocity V needs not to be corrected on the boundaries, which means that Eq. (24) can be solved with homogeneous Neumann conditions for the pressure (leading to the so-called CPPE consistent pressure Poisson equation approach⁴⁸). The logical sequence of steps is therefore: solution of Eq. (22) with the physical boundary conditions for the velocity, solution of Eq. (24) with Neumann homogeneous conditions for the pressure, and the final determination of the velocity field exploiting Eq. (23).

It is also worth recalling that the elegant compactness of these equations and the related algorithm relies on some well-known theorems, which make sure the problem is well-posed from a mathematical point of view. According to the so-called “theorem of the inverse calculus,” in a simple connected domain, a vector field can be made uniquely determined (fixed) by assigning its divergence, curl (its “vorticity” if the considered vector is the fluid velocity) and normal component at the boundary.⁴⁹ Equations (22)–(24) guarantee that $\nabla \cdot V^{n+1} = 0$ and $\nabla \wedge V^{n+1} = \nabla \wedge V^*$; i.e., the divergence and curl of the velocity field are the same that would be obtained through solution of the original set of equations, making this theorem implicitly satisfied (along these lines it is also worth recalling that the boundary conditions set for the velocity in this work always imply that the component of the velocity perpendicular to the boundary is assigned, i.e., it is zero). The decomposition of the velocity field implemented through Eq. (23) may also be regarded as a spin-off of the *Hodge or Helmholtz decomposition theorem*,⁵⁰ which states that any vector field (V^* in the present case) can always be decomposed into the gradient of a scalar function (∇p) and a solenoidal part, i.e., V^{n+1} . Additional information on this class of methods can be found in Refs. 51–55.

In the present work, convective terms have been treated using the QUICK (Quadratic Upstream Interpolation for Convective Kinematics) scheme, while standard central differences have been used to discretize the diffusive terms.

1. Validation

A validation of the fluid dynamic kernel of OpenFOAM used to solve the thermovibrational flow is available in the aforementioned

Ref. 41. A verification of the particle-tracking kernel can be found in Ref. 46, where its ability to predict correctly particle dynamics and related accumulation effects was tested against another category of phenomena, namely, the occurrence of particle accumulation structures in time-dependent thermocapillary flows (see, e.g., Melnikov and Shevtsova,⁵⁶ Gotoda *et al.*,⁵⁷ and Sakata *et al.*⁵⁸). As a third-level stage in such a multi-fold validation hierarchy, in the present study, a direct comparison is implemented between the results provided by OpenFOAM for the specific problem under investigation and those obtained using an in-house code (the same used to produce the results published in Refs. 27–31).

In particular, for consistency, such a comparison is made first between the vertical velocity signals at the center of the cavity and the Nusselt number across the hot wall of the cavity. The non-dimensional values associated with the validation case are $Pr = 7$, $Ra_w = 4 \times 10^4$, $\Omega = 50$, $\gamma = 1.25 \times 10^7$, $\xi = 1.85$, and $St = 10^{-5}$.

Figure 2 clearly confirms that, in using two different computational platforms, perfect agreement in the fluid behavior is obtained.

The validation can therefore be extended to the dispersed phase. Along these lines, the evolution of the following non-dimensional quantities is considered

$$Q^- = \frac{\sum_{v_p < 0} m_{part} v_p}{M_{tot}}, \quad Q^+ = \frac{\sum_{v_p > 0} m_{part} v_p}{M_{tot}}, \quad (25)$$

where m_{part} is the mass of the generic particle and the M_{tot} accounts for the mass of all particles dispersed in the fluid (according to this definition Q may be regarded as the mass averaged velocity possessed by all particles moving in the same direction or the average momentum per unit mass⁵⁹).

As witnessed by Fig. 3, also in this case good agreement is found between the two platforms. Indeed, the evolution in time of the global quantity Q^- is essentially the same in terms of both amplitude and frequency spectrum content. In particular, two temporal characteristics stand out from this figure: a small peak is visible just before a higher peak in Q^- .

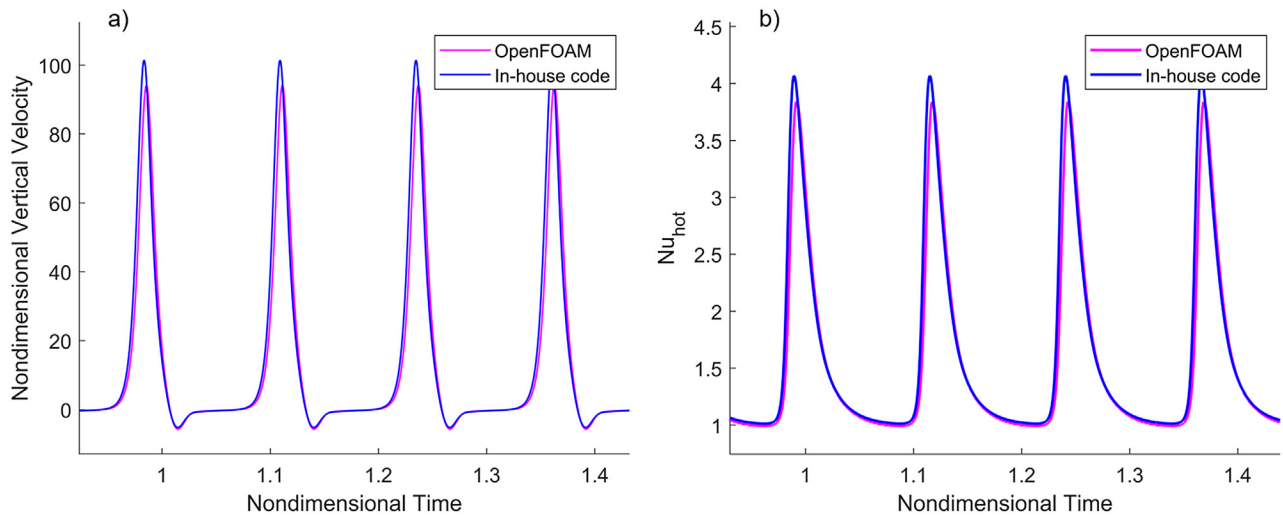


FIG. 2. Validation of OpenFOAM against in-house code for the 2D case $Pr = 7$, $Ra_w = 4 \times 10^4$, $\Omega = 50$, $\gamma = 1.25 \times 10^7$, $\xi = 1.85$, and $St = 10^{-5}$ (case with conducting sidewalls): (a) the non-dimensional vertical velocity of the fluid (v) at the center of the cavity and (b) the Nusselt number across the hot wall (Nu_{hot}).

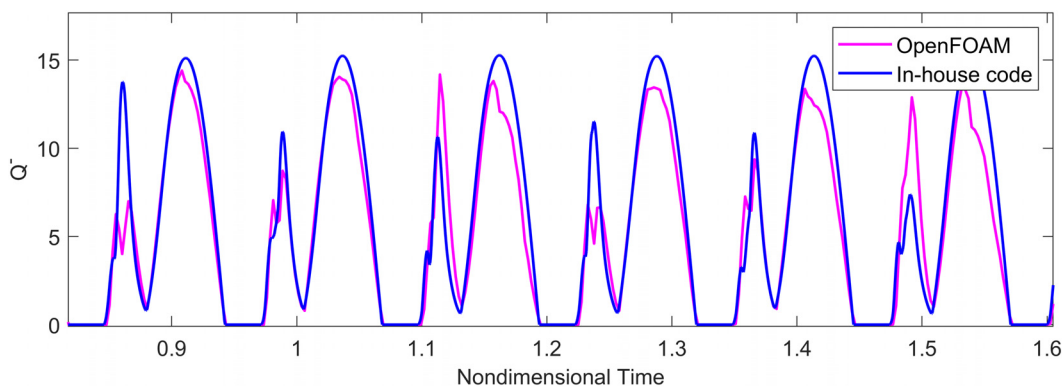


FIG. 3. Evolution of Q^- over time for $Pr = 7$, $Ra_w = 4 \times 10^4$, $\Omega = 50$, $\gamma = 1.25 \times 10^7$, $\xi = 1.85$, and $St = 10^{-5}$ (case with conducting sidewalls) obtained with OpenFOAM and in-house code.

TABLE I. Comparison of Q^- for the case $Pr=7$, $Ra_{\omega}=4 \times 10^4$, $\Omega = 50$, $\gamma = 1.25 \times 10^7$, $\xi = 1.85$, and $St = 10^{-5}$ between OpenFOAM and in-house code (case with perfectly conducting sidewalls).

	OpenFOAM	In-house	% difference
Q^-_{mean}	5.31	6.00	10.50%
Q^-_{max}	15.07	15.39	2.08%

Table I indicates that the maximum discrepancy between the two signals occurs for the value of Q^-_{max} where a difference of approximately 10% can be noticed in some cases (which we ascribe to the slightly different interpolation schemes used by the two considered solvers). Open Foam makes use of a linear weighted interpolation based on cell values, while the in-house code relies on simple linear interpolations starting from velocity component values located on the boundary of each computational cell. Figure 4 finally shows a snapshot of the particle behavior obtained using both codes at the same point in (non-dimensional) time ($t = 1.88$). In both cases, particles form a symmetrical pattern with respect to the mid-plane located at $x = 0.5$. All these observations lead to the conclusion that, as qualitatively and quantitatively substantiated by these figures, OpenFOAM and the in-house code provide essentially the same results both in terms of fluid flow and particle behavior.

2. Mesh refinement

As anticipated at the end of Sec. I, the range of non-dimensional parameters explored in this study has its origin in the previous numerical investigation by Crewdson and Lappa.⁴¹ It was shown there that

for a vibrational Rayleigh number spanning the range $8.34 \times 10^4 \leq Ra_{\omega} \leq 8.34 \times 10^5$ and a fixed angular frequency of the vibrations ($\Omega = 50$), a mesh size of 100^3 elements could produce grid-independent results in all cases. Since in this work we limit ourselves to considering the lower end of this interval, i.e., $Ra_{\omega} = 8.34 \times 10^4$, one may expect the requirement in terms of needed grid points to be smaller. Indeed, as the reader will realize by inspecting Fig. 5, grid independence is achieved for both the Nusselt number across the hot wall and the non-dimensional vertical velocity over time if an 80^3 mesh is used.

The next step of this process obviously consists of assessing whether such a numerical resolution is sufficient to obtain grid-independence in the computation of the dispersed solid phase, or not. In this regard, we refer once again to the global parameter defined before, i.e., the mass-averaged velocity of particles along the positive or negative sense of the y axis, and the outcomes of such an assessment are reported in Fig. 6. It can be seen there that although a 80^3 resolution is sufficient to guarantee mesh independence of purely fluid dynamic quantities, the density of grid points must be increased to 100^3 in order to make this requirement satisfied for the transported solid phase as well (when looking at the signal produced for both Q^- and Q^+ for the 100^3 and the 110^3 grid, almost perfect agreement is achieved). From this, it can be concluded that, although the Rayleigh number is set to a relatively small value, a grid size of 100^3 (1×10^6) elements is still required to effectively capture at the same time the fluid dynamic and the particle dynamics aspects of the problem.

IV. RESULTS

Results about the particle dynamic evolution are provided in this section for all the thermal configurations shown in Fig. 1, namely, the

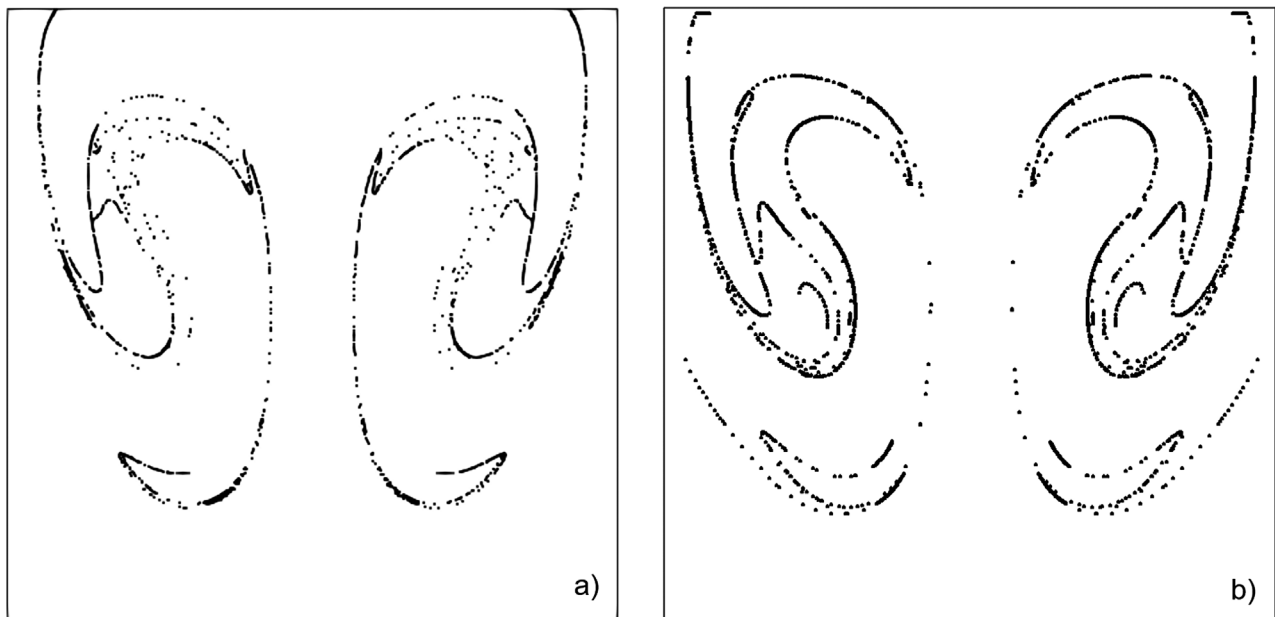


FIG. 4. Snapshots of the particle behavior for the 2D case $Pr = 7$, $Ra_{\omega} = 4 \times 10^4$, $\Omega = 50$, $\gamma = 1.25 \times 10^7$, $\xi = 1.85$, and $St = 10^{-5}$ (case with conducting sidewalls) for (a) OpenFOAM and (b) in-house code at $t = 1.88$ (non-dimensional time).

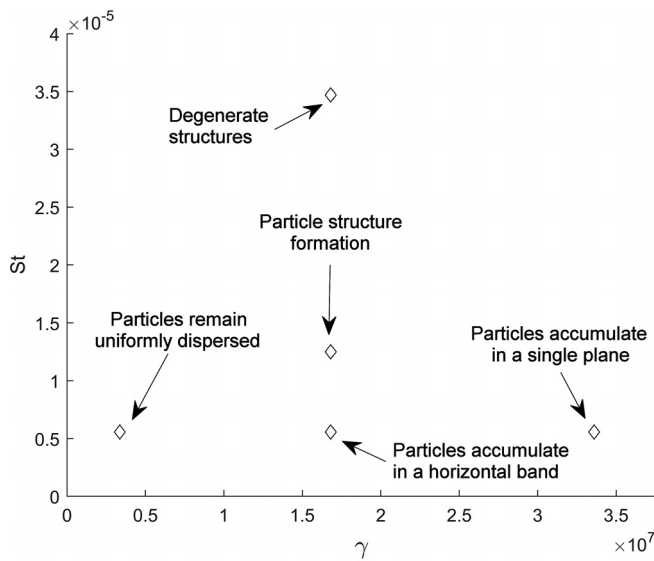


FIG. 8. Map of emerging states in the (γ, St) space of parameters.

As shown in this figure, the emerging flow typically displays a well-defined sequence of stages of evolution. In particular, two main phases or regimes can be defined in terms of relative direction of the imposed temperature gradient and acceleration produced by vibrations, one where they are concurrent (thereby supporting the onset of convection, corresponding to $t < P/2$ in Fig. 7) and one where they have opposite sign (a “stabilizing condition” corresponding to the situation where the fluid is heated from above, i.e., $t > P/2$). We wish to recall here that in terms of the strength of the flow produced accordingly in the fluid, four distinct sub-stages can be identified, namely, one in which almost quiescent conditions are maintained although acceleration has a positive sign (because convective disturbances have not been amplified yet, i.e., Stage I), a “convective burst” (where strong convection emerges as a result of the destabilizing conditions induced by the concurrent direction of acceleration and temperature gradient, Stage II), a “relaxation” phase (where the convection is strongly damped owing to the inversion in the direction of the acceleration, Stage III), and one in which no convection is present (quiescent state) because fluid flow has been suppressed during the earlier stage and the acceleration still plays a stabilizing role (Stage IV). In Ref. 41 (see Fig. 7 in that work as well), in particular, this description was made simpler by referring to the three stages in which convection is absent or relatively weak simply as “resting” or “frozen” regime.

Given this premise, yet for the convenience of the reader, the typical outcomes of the simulations conducted in the present work for the vibration acceleration and particle Stokes number spanning relatively wide intervals are synthetically reported in Fig. 8.

The significance of this initial figure resides in its ability to make evident that while trivial behaviors occur over large intervals of γ and St (states where particles simply accumulate all in a single planar surface or they remain more or less uniformly distributed in the physical domain), interesting phenomena are localized in a certain sub-region. Notably, an interpretation for the above-mentioned trivial states can be provided in a relatively simple way by considering the following

initial arguments. Particles move in the fluid as a result of two effects acting in parallel, namely, the influence of the body force (proportional to γ and ξ) acting on them due to their different density with respect to that of the fluid (a force present regardless of the existence of convective flow) and the influence of the convective flow itself (exerting on particles a drag proportional to the Stokes number). With these simple considerations in mind, the tendency of particles to retain their initial conditions (i.e., to remain uniformly dispersed in the fluid) for relatively small values of γ and St , therefore, can be simply ascribed to the too weak influence of such forces. A different explanation is needed for the other trivial states in which all particles collapse in a single plane or segments. The key to understanding such results lies in considering that while for too large values of γ , the force produced by the vibrational acceleration is so large that it leads all particles to accumulate along the solid walls of the cavity perpendicular to it (regardless of the presence of convective flow), in the other limiting conditions in which the Stokes number is very large, the particle dynamics are essentially dominated by drag effects. This explains why in the following we concentrate on intermediate values of the vibration acceleration and particle Stokes number, namely, $\gamma = 1.68 \times 10^7$ and $St = 1.25 \times 10^{-5}$, where the relative importance of the above-mentioned concurrent effects or forces is expected to be comparable, whereas the (trivial) dynamics obtained in the other cases are no longer discussed.

A. Evolution of Q^+ and Q^-

Before starting to deal with the particle patterning behavior, in order to get a clear idea of the system dynamics from a global (ensemble) point of view, it is convenient to initially assess the response of the system using the global quantities already defined in Sec. IV. Along these lines, Fig. 9 shows the temporal evolution of Q^+ and Q^- for both the light and heavy particles, for the three variants of thermal boundary conditions assumed in this study.

As qualitatively substantiated in this figure, a somehow repetitive behavior can be discerned for both Q^- and Q^+ in all cases. Indeed, apparently the particles closely follow the convective burst. As already explained before, purely fluid dynamic aspects and related patterning behaviors have already been described in Ref. 41 and such a treatment is not duplicated here for the sake of brevity. In order to interpret properly the corresponding dynamics in terms of solid mass displacement, however, it is necessary to recall that the fluid response is of type SY-P; i.e., the fluid flow is both synchronous and periodic with respect to the external forcing (the vibrations). More specifically, the fluid remains in almost quiescent conditions over a relatively long portion of the vibration period (the aforementioned resting or frozen regime) and it is then disturbed by a convective burst, characterized by a peak in terms of vertical (along y) fluid velocity. An effective example of these events is presented in Fig. 10 where the yellow dashed line represents the acceleration applied to the cavity.

A first understanding of the ensemble particle dynamics can be obtained by comparing the behavior of the light particles in Figs. 9(a) and 9(b). Notably, the negative and positive peaks occur for both Q^- and Q^+ , respectively, at approximately the same time in the period of vibrations for all three boundary conditions. At first, this may seem counterintuitive as the particles should either rise or fall depending on the direction of the vibration (i.e., if $Q^+ = 0$, then $Q^- < 0$, and if $Q^+ > 0$, then $Q^- = 0$). However, this non-trivial behavior displayed by particles should be taken as a cue to recall an important concept,

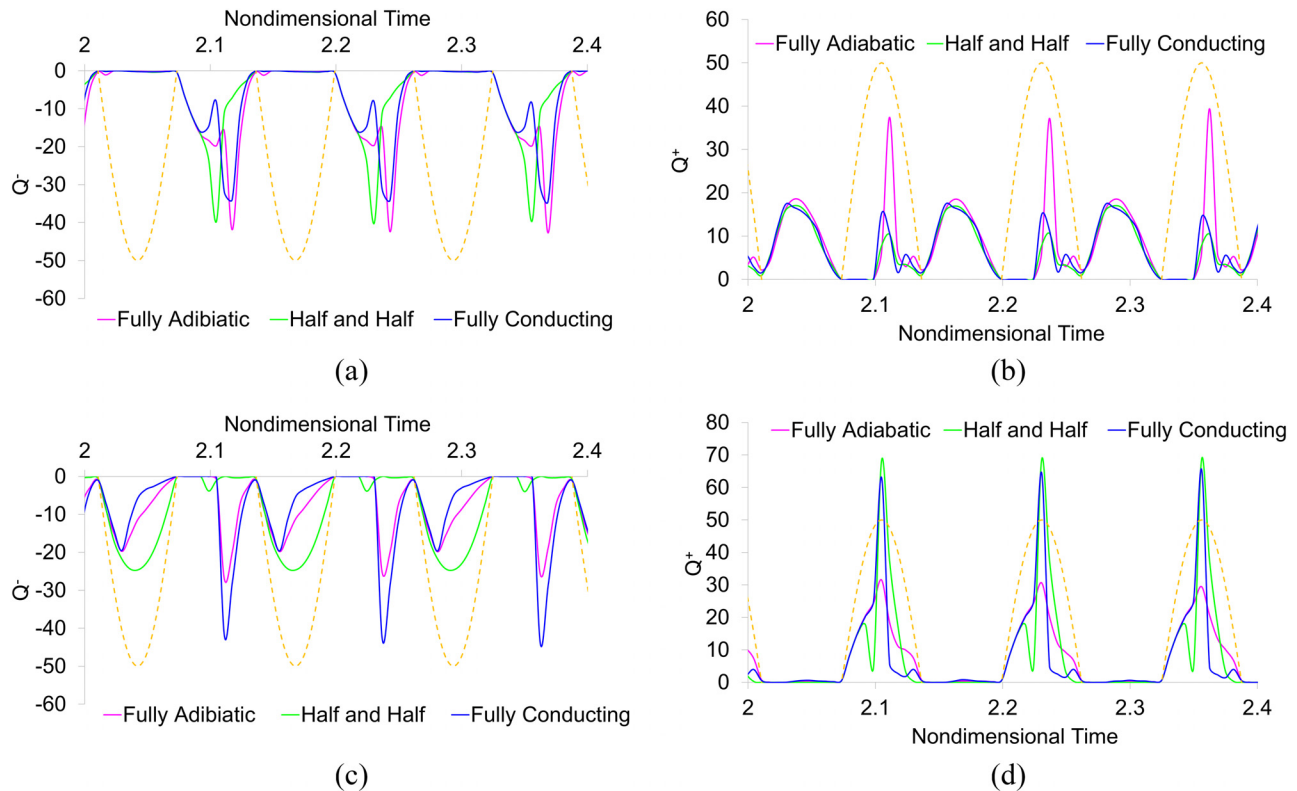


FIG. 9. Evolution of Q^- and Q^+ over time for the case $Pr = 7$, $Ra_{ov} = 8.34 \times 10^4$, $\Omega = 50$, $\gamma = 1.68 \times 10^7$, and $St = 1.25 \times 10^{-5}$ for all three boundary conditions (the yellow dashed line represents the acceleration applied to the cavity for the given non-dimensional frequency $\Omega = 50$): (a) Q^- for $\zeta = 0.3$, (b) Q^+ for $\zeta = 0.3$, (c) Q^- for $\zeta = 1.85$, (d) Q^+ for $\zeta = 1.85$.

namely, that given the presence of convection, particles do not simply travel in a rectilinear fashion as they would do in a quiescent fluid under the effect of vibrations. Rather, they do interact with the carrier flow. In earlier studies,⁴¹ it has been shown that these convective bursts often lead to the formation of single or multiple competing rolls in the fluid, with parcels of fluid traveling in certain directions depending on their location in the cavity. When particles are added to these fluid systems, they are transported either up or down, depending on their location in the cavity, which explains in a relatively simple way why Q^- and Q^+ experience concurrent signal peaks (see Fig. 11).

Other useful information, stemming from the comparison of Figs. 9(a) and 9(b) and the peaks experienced by Q^+ and Q^- , concerns a set of general rules or predictive links that can be introduced to connect the Q behavior to the slope (ψ) of the acceleration $g(t)$ applied to the cavity for each particle density. These laws, summarized in Table II, hold true for all three thermal boundary conditions.

Another key observation relates to the similarities appearing between the responses of Q^+ for $\zeta = 0.3$ and Q^- for $\zeta = 1.85$ [Figs. 9(b) and 9(c), respectively], and between Q^- for $\zeta = 0.3$ and Q^+ for $\zeta = 1.85$ [Figs. 9(a) and 9(d), respectively]. An explanation/justification for this trend can be elaborated in its simplest form on the basis of the argument that the light and heavy particles are expected to behave in a quasi-polar opposite manner. This affinity is captured in Fig. 12, where Q^+ for $\zeta = 0.3$ and Q^- for $\zeta = 1.85$ are superimposed for the case

where all sidewalls are adiabatic. A similar agreement is found for the signals of Q^- for $\zeta = 0.3$ and Q^+ for $\zeta = 1.85$ (not shown).

On a separate note, it is also worth highlighting that although the trends for the different boundary conditions are relatively similar, some interesting differences exist. Further inspection of Fig. 9 is useful in this regard (in pink: fully adiabatic sidewalls, in green: hybrid thermal configuration, and in blue: perfectly conducting sidewalls). The first discrepancy affects the situation where the two sidewalls are conducting and the front and back are adiabatic. In such a case, there is little to no negative particle momentum (Q^-) when the heavy particles are considered for $\psi < 0$ and $g(t) > 0$. When recalling the similarities between Q^- for $\zeta = 1.85$ and Q^+ for $\zeta = 0.3$, the positive momentum for the case Q^+ for $\zeta = 0.3$ for $\psi < 0$ and $g(t) > 0$ is also much lower than for the other two thermal boundary conditions. The reason for such a behavior resides in the fact that, as shown by previous work,⁴¹ for this range of parameters and thermal boundary conditions, the flow is more stable with respect to the circumstances where all walls are set to either adiabatic or conducting. Although the flow still undergoes a convective burst at a given point in the period, the patterning behavior of the fluid in the resting regime (i.e., when the fluid is quasi-stationary and the fluid velocity is close to zero) does not contain as many rolls as in the other cases.⁴¹ During this stage, no toroidal rolls are visible as the structure simply reduces to a planar extension of the so-called 2D quadrupolar field.

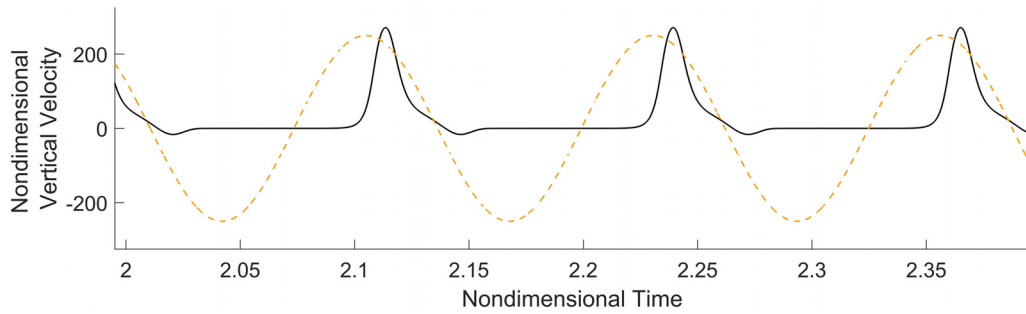


FIG. 10. Non-dimensional vertical velocity (v) for the case where all sidewalls are adiabatic. The yellow dashed line represents the acceleration applied to the cavity.

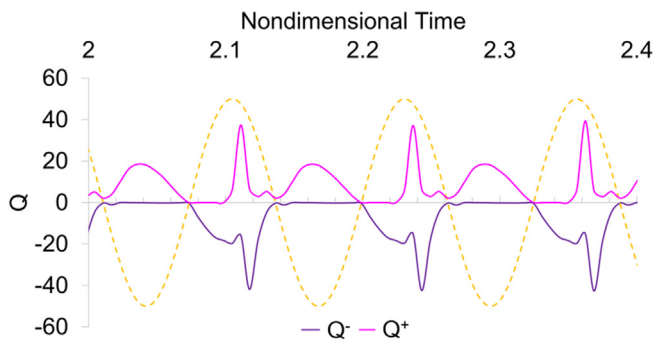


FIG. 11. Evolution of Q^- and Q^+ over time for $\xi = 0.3$ and the case where all sidewalls are adiabatic. The yellow dashed line represents the acceleration applied to the cavity.

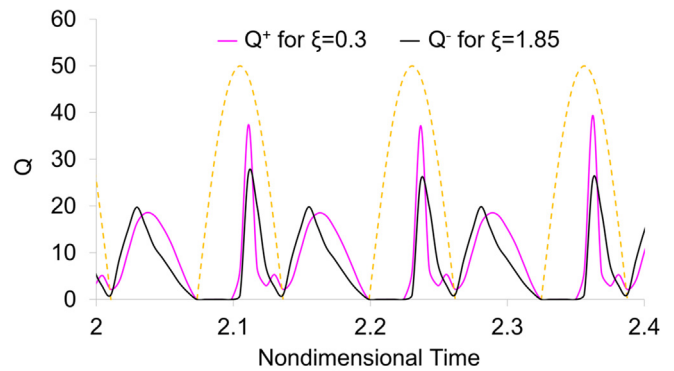


FIG. 12. Evolution of Q^+ for $\xi = 1.85$ (black) and Q^- for $\xi = 0.3$ (magenta) over time, for the case where all sidewalls are adiabatic. The yellow dashed line represents the acceleration applied to the cavity.

TABLE II. Parameter Q behavior as a function of the acceleration.

ξ	ψ	$g(t)$	Q^-	Q^+
0.3	>0	<0	$=0$	>0
0.3	>0	>0	<0	$=0$
0.3	<0	>0	<0	>0
0.3	<0	<0	$=0$	>0
1.85	>0	<0	<0	$=0$
1.85	>0	>0	$=0$	>0
1.85	<0	>0	<0	>0
1.85	<0	<0	<0	>0

TABLE III. Maximum absolute values of Q^- (top panel) and Q^+ (bottom panel) for all three boundary conditions.

	ξ	Adiabatic	Half and half	Conducting
$ Q^+ $	0.30	39.82	16.99	17.30
	1.85	31.52	68.33	65.50
$ Q^- $	0.30	43.38	42.05	35.90
	1.85	27.40	24.63	43.90

As the next step of this analysis hierarchy, it is worth comparing the maximum absolute values of Q^- and Q^+ for each case (Table III). Starting with the negative particle momentum (Q^-), for the light particles ($\xi = 0.3$), it can be seen that all three boundary conditions return a similar maximum value of $|Q^-|$, whereas, for the heavy particles, the value of $|Q^-|$ is much higher in the situation where all sidewalls are conducting. Looking at the positive particle momentum (Q^+), the difference in maximum values of $|Q^+|$ is more pronounced, both when

the particle density and the boundary conditions are changed. Particularly, the maximum negative momentum of the light particles is much lower than for the heavy particles in the hybrid configuration case or when all sidewalls are conducting.

From this in-depth quantitative analysis of the general behavior of the particles dispersed in each of the three considered systems, some general conclusions can be drawn. First, the particle structures are disturbed periodically and synchronously with respect to the applied forcing. The only exception is the hybrid (“half and half”) case, owing to the inherent stability of the fluid flow. Second, the overall momentum of the light particles and the heavy particles behaves similarly when the negative momentum of one is compared to the

positive momentum of the other. This however does not translate to a similarity in maximum momentum amplitude. An interpretation of this specific aspect is not as straightforward as one would assume and requires a detailed analysis of the particle spatiotemporal evolution and patterning behavior, which is elaborated in Sec. IV B.

B. Temporal evolution of particle structures

Given the similarities in the system evolution when different thermal boundary conditions are considered (Sec. IV A), here, without loss of generality and for brevity, the treatment is limited to the case with conducting sidewalls (Figs. 13 and 14).

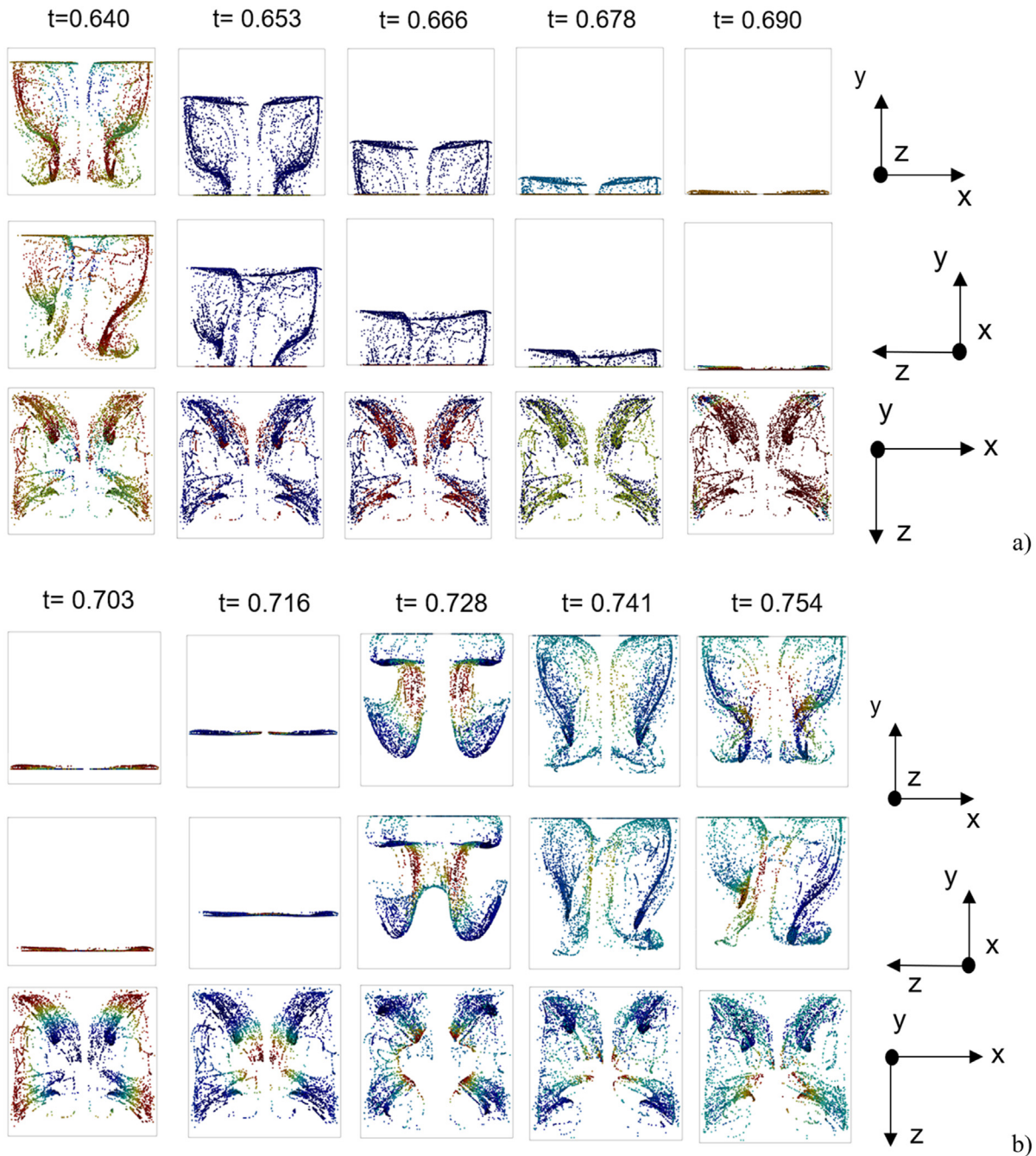


FIG. 13. Temporal evolution of the particle distribution over one vibrational period for $\zeta = 1.85$, where t is the non-dimensional time and the vibrational period has been divided into ten snapshots evenly spaced in time (conducting sidewalls case). The blue color indicates a low vertical velocity, and the red color indicates a high vertical velocity: (a) $0.640 \leq t \leq 0.690$, (b) $0.703 \leq t \leq 0.754$.

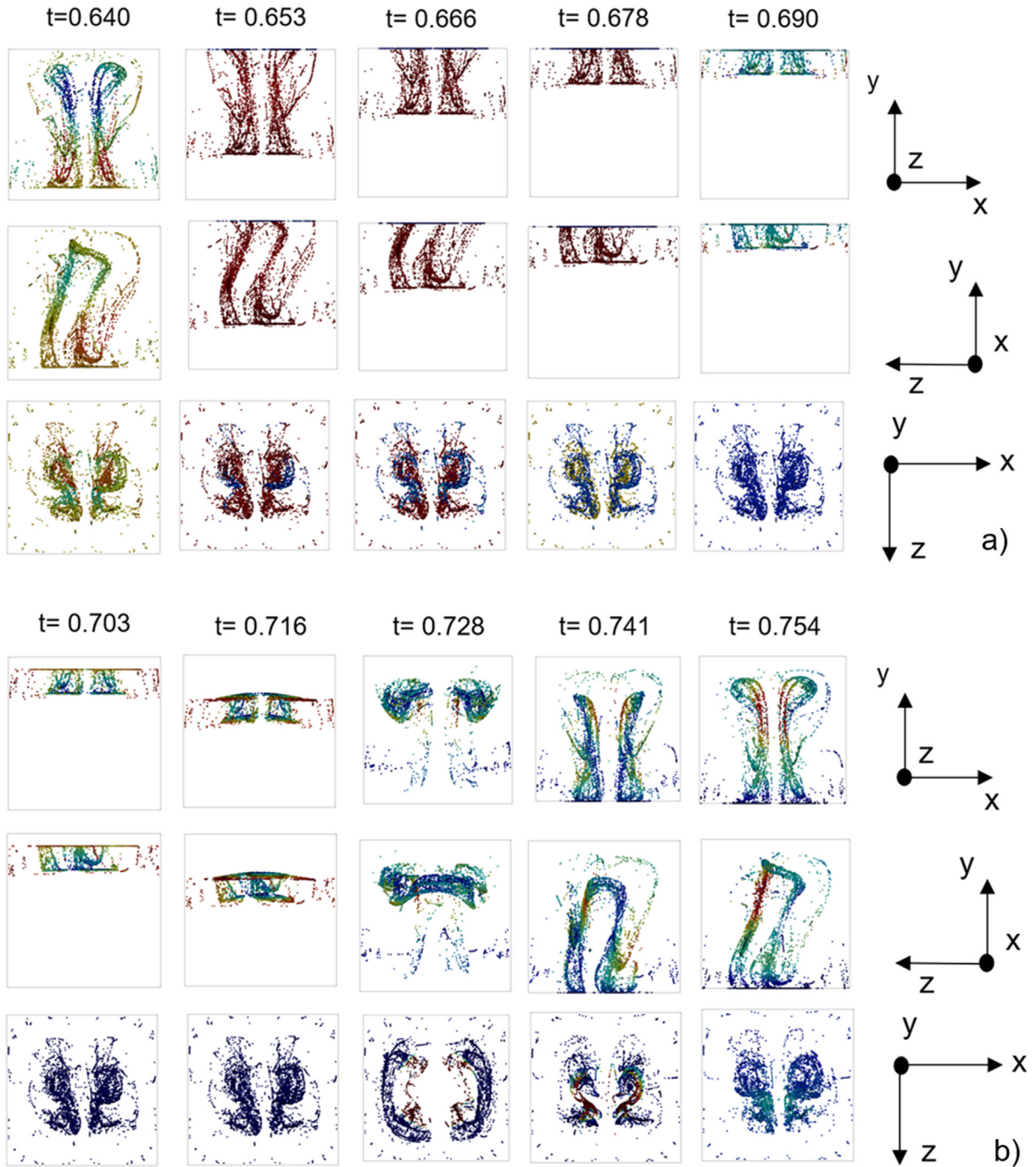


FIG. 14. Temporal evolution of the particle distribution over one vibrational period for $\zeta = 0.3$, where t is the non-dimensional time and the vibrational period is divided into ten snapshots evenly spaced in time (conducting sidewalls case). The blue color indicates a low vertical velocity and the red color a high vertical velocity: (a) $0.640 \leq t \leq 0.690$, (b) $0.703 \leq t \leq 0.754$.

In such a context, the first figure of the sequence [Fig. 13(a)] is extremely instructive as it shows that in the time interval from $t = 0.640$ to $t = 0.690$, the particle distribution evolves from a scenario where it fully occupies the entire fluid domain to one where the

structure is compressed in the negative y direction, until a stage is attained where all particles lie on the bottom of the cavity. This compression occurs when the acceleration $g(t)$ is negative. In this time-frame, the velocity of the fluid is *relatively small or completely*

negligible in the entire cavity; this interval corresponds to the aforementioned “flow damping stage” (Stage III) followed by the “quiescent phase” (Stage IV, see again Fig. 7). The body force acting on the particles (due to the acceleration induced by vibrations and their different density with respect to the carrier fluid) is therefore dominant in this stage and, as a result, all particles accumulate forming a planar structure attached to the bottom wall.

In the next five instances, from $t = 0.703$ to $t = 0.754$ [Fig. 13(b)], the particles transition from a downward motion to an upward one as $g(t)$ changes its sign; i.e., it becomes positive. This inversion in the acceleration direction results in the aforementioned compressed (planar) structure detaching from the bottom wall and traveling upward. In the snapshots pertaining to $t = 0.703$ and $t = 0.716$, the layer of particles travels up following this detachment (this time interval corresponds to the “almost quiescent conditions,” i.e., Stage I indicated in Fig. 7), until the time $t = 0.728$, where the convective burst occurs (corresponding to Stage II in Fig. 7). In such conditions, the particle layer is disrupted due to the viscous force (the aforementioned particle drag) that the emerging flow exerts on particles. Finally, at $t = 0.754$ the fluid returns to its resting configuration and the same concept applies to the particle distribution.

Figure 13 is naturally complemented by Fig. 14, where the fluid and system properties remain the same, but the light particles are considered. In these circumstances, as expected, the dispersed solid mass behaves in the opposite way with respect to the heavy case. The structure is compressed in the positive y direction when the acceleration $g(t)$ is negative and migrates in the negative y direction when the acceleration changes its sign. As an appreciable distinguishing mark, however, the distribution of solid matter is not compressed along the wall as much as the heavy particle case. This confirms that the particle density does play a role in the compressibility of the particle velocity field. At this stage, it should also be recalled that the carrier flow underpinning the particle dynamics shown in Figs. 13 and 14 is exactly the same and it is not affected by dispersed solid mass in the frame of a one-way coupling approach. This supports the straightforward conclusion that the visible differences relate only to the properties of the particles and their transport mechanisms.

All these behaviors are summarized in Fig. 15, which provides a general overview of the evolution of the solid mass distribution in the different characteristic stages defined for the fluid flow for both heavy and light particles. These and the underlying cause-and-effect relationships can be synthetically sketched as follows:

Stage I: The acceleration $g(t)$ is positive; however, convection has not been produced yet as the convective disturbances take some time to be excited and amplified accordingly; the flow is in quiescent (or almost motionless) conditions and particles only feel the force acting on them due to the acceleration $g(t)$ and their different density with respect to the surrounding fluid; as a result, the planar structure containing heavy (light) particles migrates upward (downward).

Stage II: A plume of fluid is produced owing to the excitation of buoyant flow. Convection is so strong that the drag exerted on particles becomes the dominant force. Accordingly, an eruption of particles originates from the planar structure, which is totally destroyed by such an effect.

Stage III: The acceleration $g(t)$ becomes negative and, at the same time, the existing convective flow is strongly mitigated. Particles

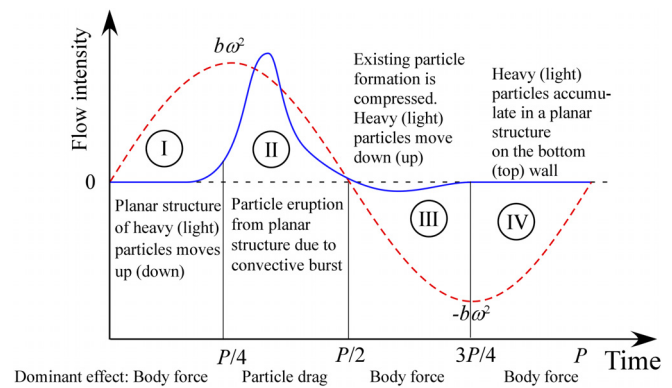


FIG. 15. Sketch of the typical stages of evolution of the particles subjected to an acceleration varying sinusoidally in time in a direction parallel to the imposed temperature gradient (flow magnitude—blue solid line, acceleration—red dashed line, $P = 2\pi/\Omega$).

move accordingly essentially under the influence of the density-induced body force. The particle formation produced by the eruption occurred in Stage II is progressively flattened.

Stage IV: The fluid is in a completely convection-less state. The body force is the only active force and it pushes all the heavy (light) particles toward the bottom (top) wall where they accumulate forming again a planar structure.

In the following, some additional detailed information is also provided to clarify the specific particle dynamics evolved during the convective burst (Stage II). In this phase, the flow evolves as a plume directed along the y axis (fluid moving in the negative y direction in the center of the cavity), which undergoes some textural transitions as time passes. Such evolution, shown in detail in Fig. 16, has already been extensively described in Ref. 41, and for this reason, here we limit ourselves to observing that, as a result of the modification in the shape of such a convective plume, the distribution of particles is modified accordingly (see the correspondence between the flow in Fig. 16 and particle structures in Figs. 17 and 18 for the heavy and light particle cases, respectively).

Other interesting insights into these dynamics stem once again from a comparison of the situations with heavy and light particles. Indeed, the different morphologies of the particle formations visible during the convective burst for $\zeta = 1.85$ and $\zeta = 0.3$ depend not only on the different position and direction in which the planar particle structure is moving at the time when the convective burst is enabled, but also on the different way with which particles react to the thermal plume (i.e., the central jet of fluid) and the related toroidal roll.

In the heavy particle case [see Figs. 13(b) and 17 for $t = 0.716$], the initial position of the particle planar structure is relatively close to the bottom wall and it is moving upward. Owing to the interaction of the particles with the central jet of fluid, a formation is created which essentially protrudes into the clear fluid located under the planar structure [see Figs. 13(b) and 17 for $t = 0.728$]. At later times ($t = 0.741$ and $t = 0.754$), “lobes” are formed due to the recirculation of particles in the toroidal roll associated with the plume, which tends to transport particles back toward the top wall. In this case, particles are displaced upward in proximity to the sidewalls of the cavity due to the joint

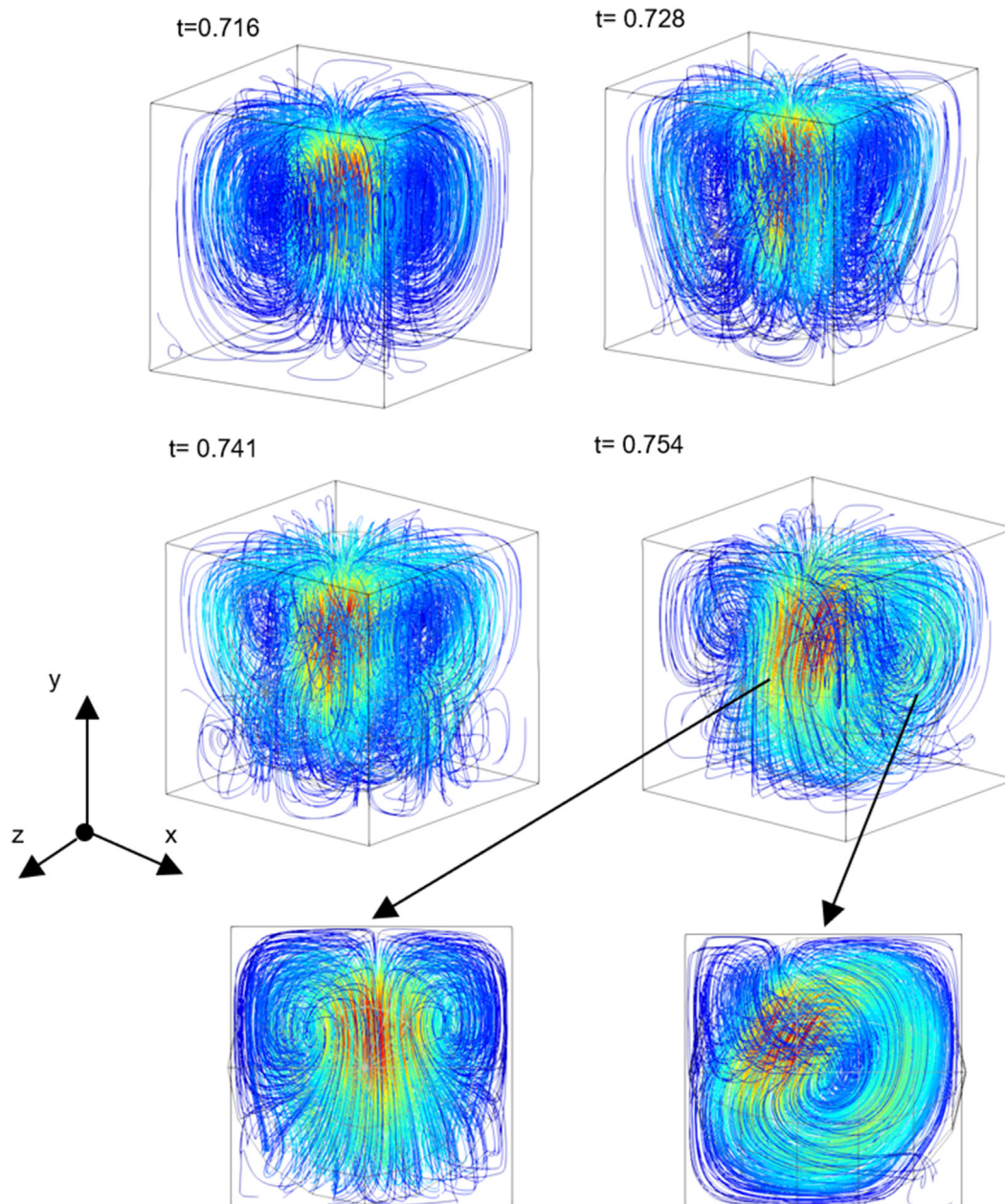


FIG. 16. Snapshots of the flow field at different times during the convective burst stage. (conducting sidewalls case). The blue color indicates a low vertical velocity, and the red color indicates a high vertical velocity.

influence of the body force induced by the acceleration and the drag exerted on particles by the moving fluid.

If the light particles are considered [see Figs. 14(b) and 18 for $t = 0.716$], the initial position of the planar structure is completely different. It is initially located in proximity to the top wall. Moreover, it migrates in the downward direction. As the central jet of fluid moves in the same direction, a very evident central eruption of particles

moving downward is produced, whereas the lobe-formation effect described for the heavy-particle case is strongly mitigated [the tendency of particles to rise along the sidewalls due to their interaction with the related rising fluid is hindered by the particle buoyancy effect, which keeps pushing them toward the bottom wall; accordingly, particle formations with a smaller radial extension are obtained, Figs. 14(b) and 18].

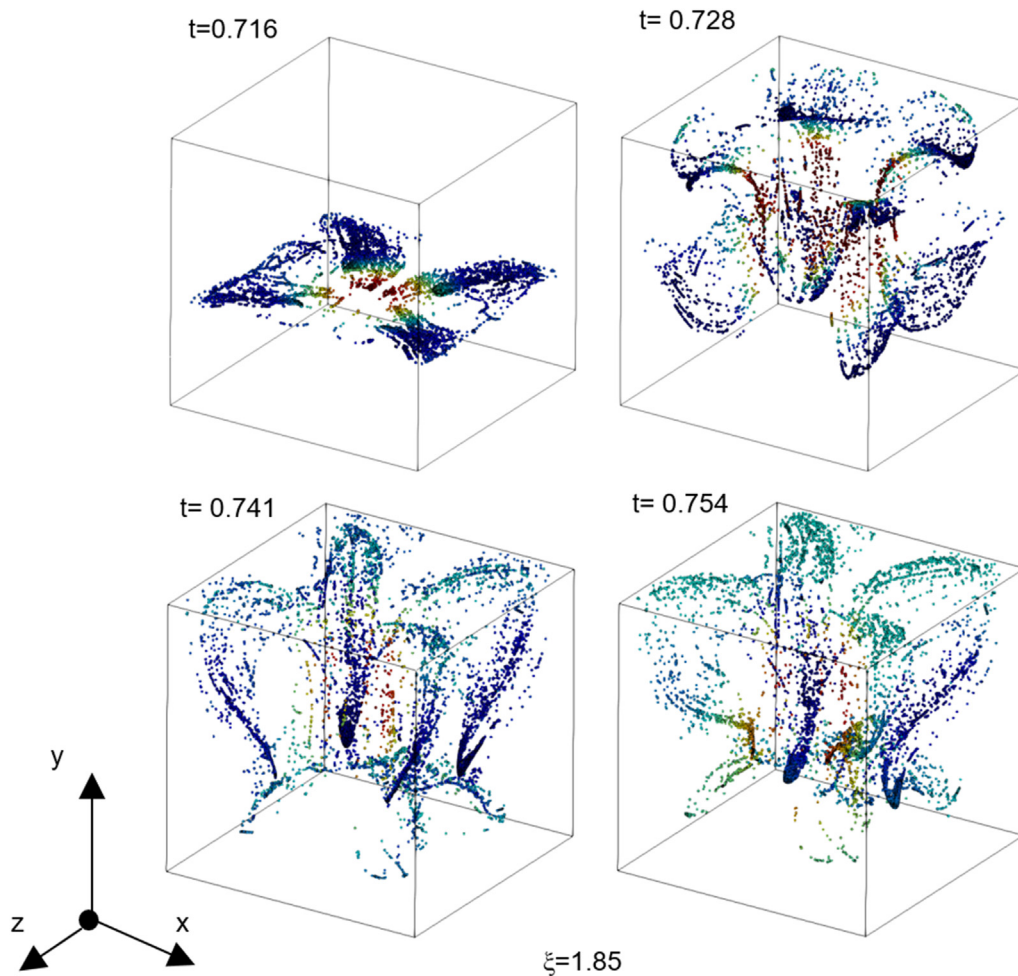


FIG. 17. Snapshots of heavy ($\xi = 1.85$) particle distribution at the same times shown in Fig. 16.

Having completed a description of the particle patterning behavior for a representative case, Sec. IV C is devoted to an assessment of the differences in structure morphologies obtained when the thermal boundary conditions are varied. A change in the thermal boundary conditions, indeed, induces appreciable modifications in the shape of the plume emerging during the convective burst (Stage II, the reader being referred again to Ref. 41 for a detailed treatment of this aspect). Such variations are reflected by (or reverberated into) corresponding changes displayed by the particle formations (as illustrated in detail in Sec. IV C).

C. Morphological dependence of the particle distribution on the imposed thermal boundary conditions

Selected examples of the 3D dynamics obtained with different thermal boundary conditions are collected in Figs. 19–27. In particular, one snapshot is reported for each case at the time just after the occurrence of the convective burst, i.e., when the resting regime is

entered. Starting with the thermal configuration where all the sidewalls are adiabatic (the reader being referred to Fig. 8 in Ref. 41 for the corresponding 3D flow field), Fig. 19 refers to the light particles case ($\xi = 0.3$).

By providing a good impression of the overall three-dimensional distribution of dispersed solid mass, this figure is instrumental in showing that the related morphology takes on a *mushroom*-like configuration, where two bulk structures are visible. The two lobes are almost perfectly symmetrical about the zy mid-plane and are separated by a region of clear (particle-free) fluid located at $x = 0.5$.

Additional insight follows naturally from a comparison of Figs. 19 for $\xi = 0.3$ and 20 for $\xi = 1.85$. The spatial configuration of the particle structures is similar. However, in the latter case, the area occupied by the particles within the cavity is much larger and its shape is more defined or recognizable. For the convenience of the reader, a direct superposition of these particle formations is presented in Fig. 21.

The next set of figures of the sequence illustrates the situation where two opposing sidewalls of the cavity are perfectly conducting,

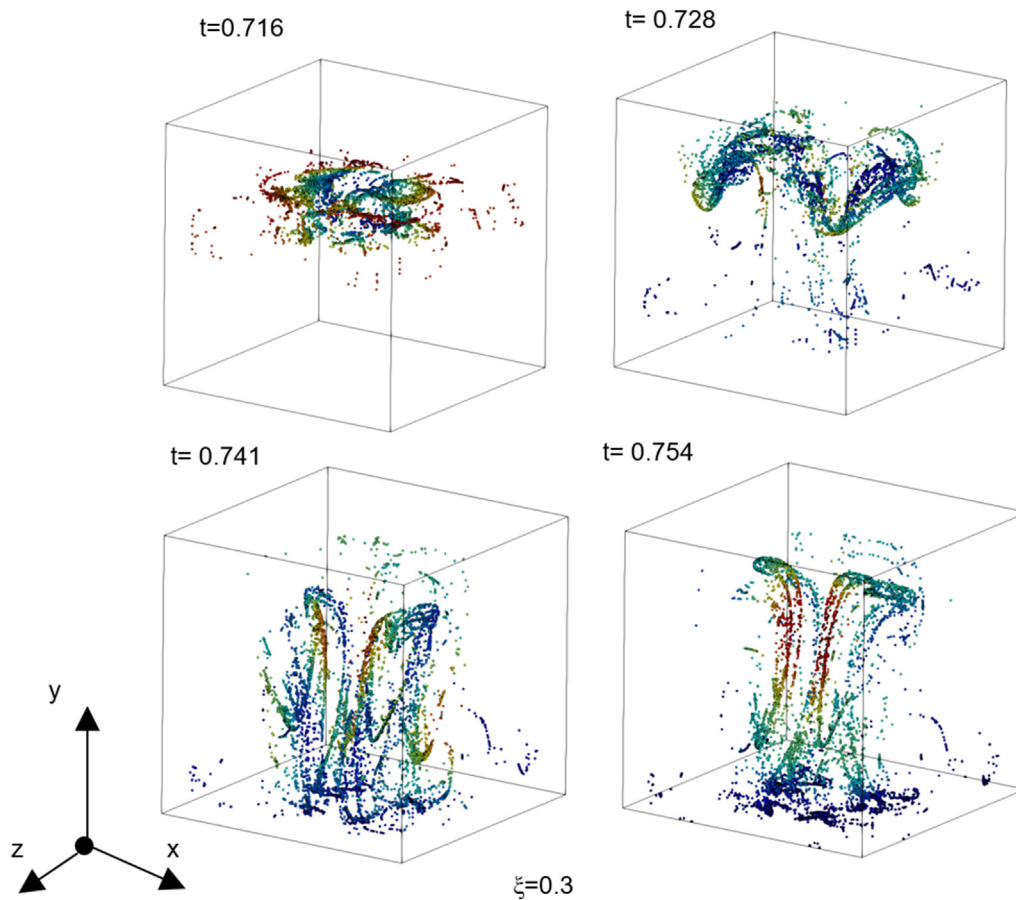


FIG. 18. Snapshots of light ($\xi = 0.3$) particle distribution at the same times shown in Fig. 16.

while the other two walls are adiabatic (hybrid case, the reader being referred to Fig. 12 in Ref. 41 for the corresponding 3D flow field). In particular, Figs. 22 and 23 deal with the density ratios $\xi = 0.3$ and $\xi = 1.85$, respectively. Taken together (the reader being also referred to the direct cross-comparison implemented in Fig. 24), these snapshots indicate that the formation in the heavy particle case is much more compact than the other. Both are much more symmetrical than those seen in the adiabatic wall case.

As a concluding step of such a discussion, a description of the corresponding dynamics for the configuration where all sidewalls are conducting is needed. Along these lines, Fig. 25 shows the pattern for the light particles. Two lobes, symmetrical about the zy mid-plane, are visible and occupy the top section of the cavity. A concave morphology can be seen on their undersides. Similarly to the case where all sidewalls are adiabatic, a slight asymmetry is visible about both mid planes of the x axis and z axis. This becomes evident when looking at the top view in Fig. 25.

For the heavy particles, Fig. 26 reveals a structure that bares much similarity to the fully adiabatic case.

To complement this scenario with additional relevant data, further examination of the formations visible in Fig. 21 with respect to

those revealed by Fig. 27 (dealing with the situations where walls are fully adiabatic and fully conductive, respectively) leads to another key realization; namely, it provides evidence for the more symmetric nature of the particle distribution shown in red in Fig. 27 (side view). When the light particles are considered (green symbols), the main dissimilarity concerns the extension of the formations in the $-y$ direction. Indeed, for the case with the adiabatic walls, the aforementioned *mushroom* structure is visible, whereas for the companion situation where all walls are conducting, the fingerprint of the particle structure is its compact nature and the tendency of all particles to reside in the top half on the cavity.

V. DISCUSSION AND CONCLUSION

Through consideration of a situation as conceptually simple as that of a dilute distribution of solid finite-size (spherical) particles undergoing thermovibrational effects in a differentially heated cubic container, it has been shown that the ability of this type of flow to support particle clustering phenomena is not an exclusive prerogative of systems where vibrations have a component acting in a direction perpendicular to the imposed (unidirectional) temperature gradient. Although the most common outcome of the configuration with

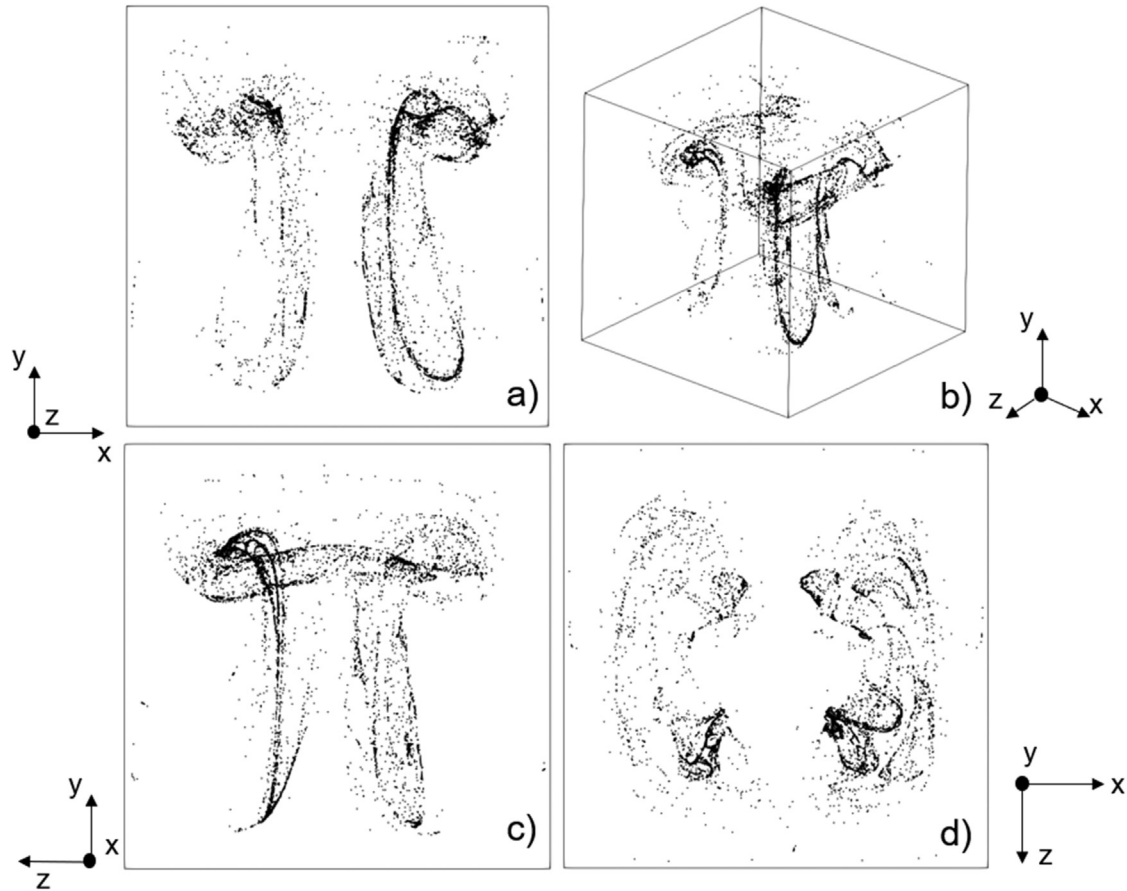


FIG. 19. Particle morphology for the case of fully adiabatic sidewalls, $\xi = 0.3$ and $t = 2.364$: (a) xy view, (b) 3D view, (c) yz view, (d) xz view.

vibrations perfectly parallel to the temperature gradient for relatively high values of the non-dimensional acceleration amplitude is a degenerate state in which all the dispersed solid mass accumulates in a perfectly planar surface that moves back and forth between the hot and cold sides of the cavity, specific conditions can be identified for which particles are forced to demix from the liquid and give rise to structures with well-defined (non-trivial) morphological properties. These range from mushroom-like 3D surfaces to much more compact realizations depending on the particle-to-fluid density ratio and the specific thermal boundary conditions implemented for the sidewalls of the enclosure.

Such formations show up or exist as relatively stable entities during limited sub-intervals of the vibration period. First, the particle distribution is frozen in the cavity; then, it is compressed to the bottom or top wall and then detaches when the acceleration changes direction. As a convective burst occurs, the “flat” particle distribution is disrupted by the increase in the strength of the flow, and then, it regains its original frozen configuration, thereby giving rise to an endless series of cycles where well-defined structures are continuously created and destroyed. This confirms that the behavior of the particle distribution is synchronous and periodic (SY-P) in accordance with the regime

associated to the carrier fluid. This transition of states is ubiquitous for all cases, irrespective of the considered thermal boundary conditions at the sidewalls.

Comparison with the companion category of particle attractors investigated by Lappa and co-workers^{27–34} indicates that, although these phenomena display some affinities in terms of driving forces or effects, notable dissimilarities exist. Both are driven by the joint action of thermovibrational convection and particle inertial effects. What sets the case with parallel vibrations apart from that with perpendicular ones resides essentially in the spatiotemporal nature of the phenomena and the specific relationship that is established between fluid motion and particle density-related effects. In the perpendicular case, particle clustering is a continuous process by which dispersed solid mass continuously separates from the fluid and accumulates along well-defined structures, which grow in time until an asymptotic state is attained in terms of shape and size. The related morphology depends essentially on the direction of vibrations with respect to the walls of the cubic cavity, possible shapes being paraboloids, conical surfaces, ellipsoids, cylinders, spheres, etc. The related morphology can be considered “stationary” in the sense that the final formations move back and forth along the direction of vibrations thereby giving an external observer

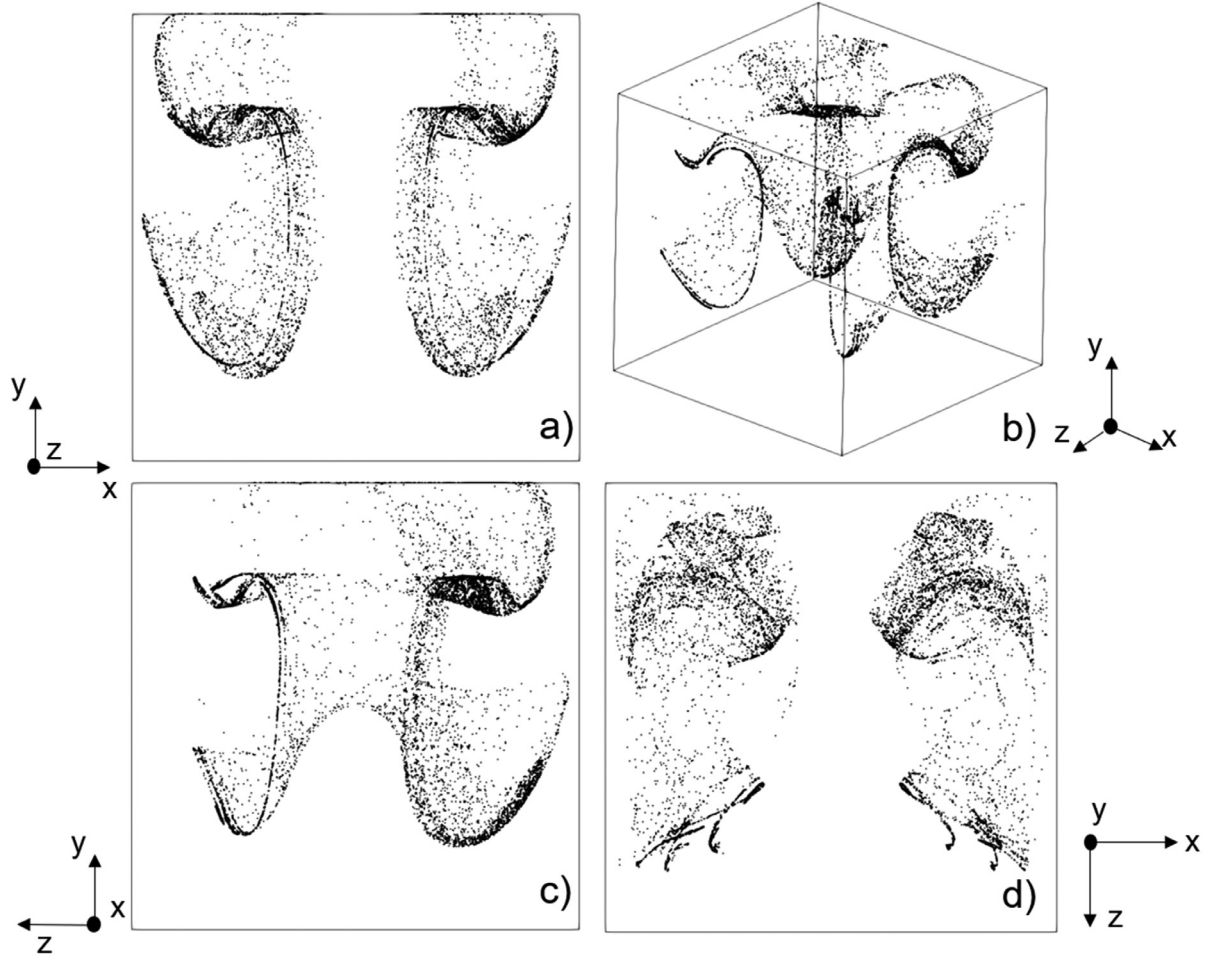


FIG. 20. Particle morphology for the case of fully adiabatic sidewalls, $\zeta = 1.85$ and $t = 2.364$: (a) xy view, (b) 3D view, (c) yz view, (d) xz view.

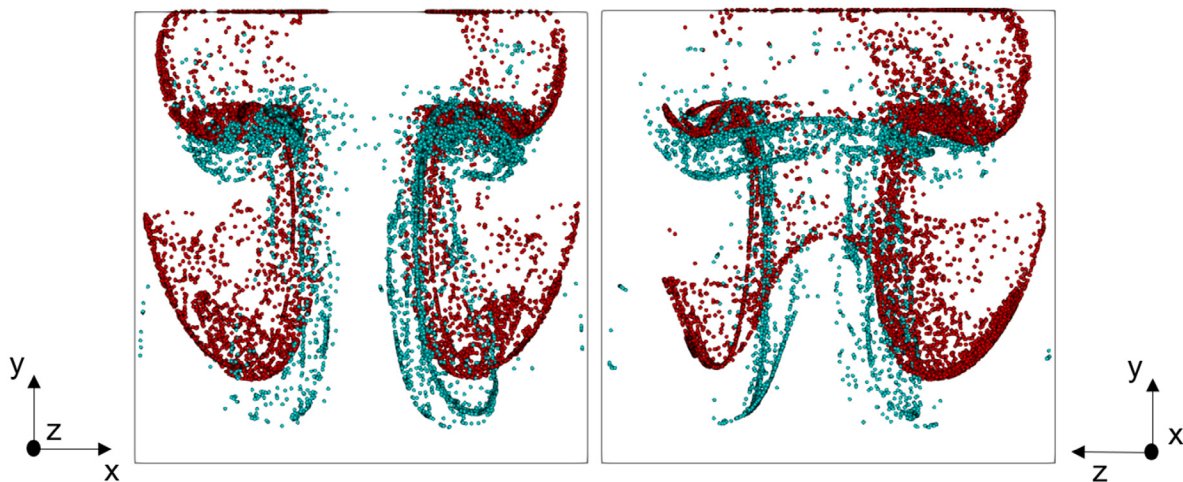


FIG. 21. Superposition of the particle distribution for $\zeta = 0.3$ (in green) and $\zeta = 1.85$ (in red) for the case of fully adiabatic sidewalls, and $t = 2.364$. Front view (left) and side view (right).

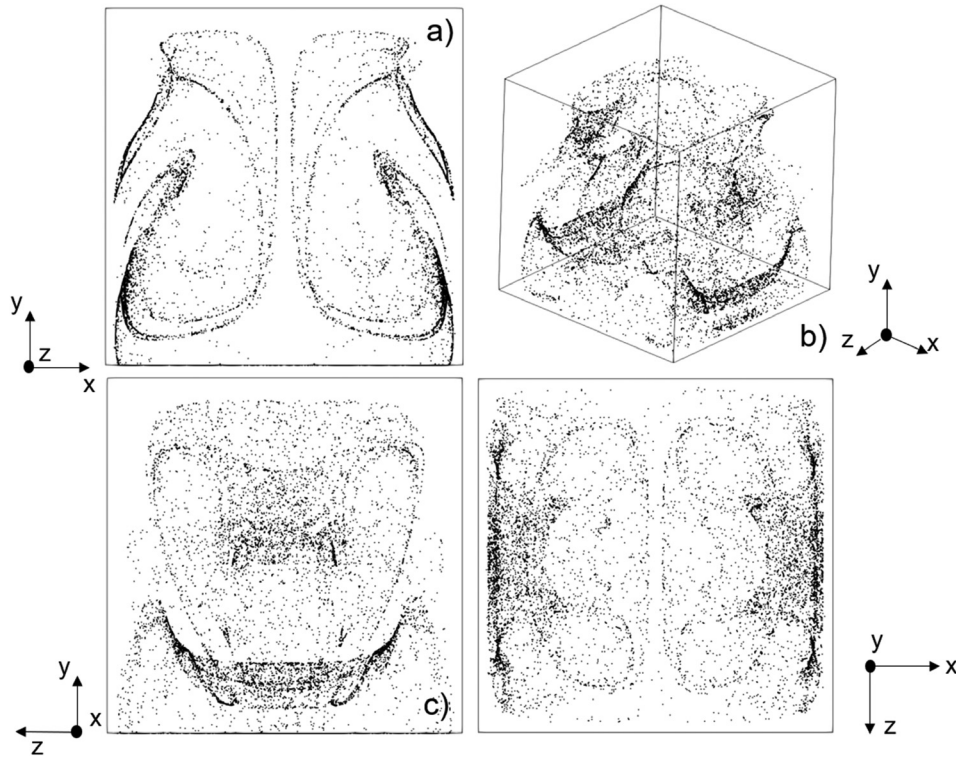


FIG. 22. Particle morphology for the case of conducting sidewalls and adiabatic front and back walls, $\zeta = 0.3$ and $t = 2.364$: (a) xy view, (b) 3D view, (c) yz view, (d) xz view.

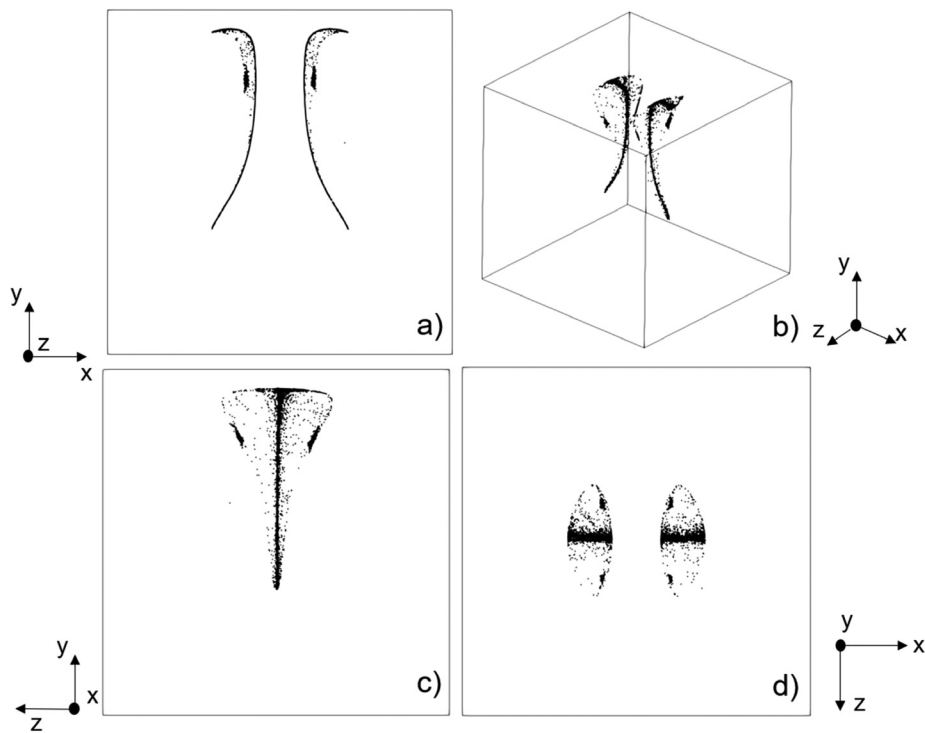


FIG. 23. Particle morphology for the case of conducting sidewalls and adiabatic front and back walls, $\zeta = 1.85$ and $t = 2.364$: (a) xy view, (b) 3D view, (c) yz view, (d) xz view.

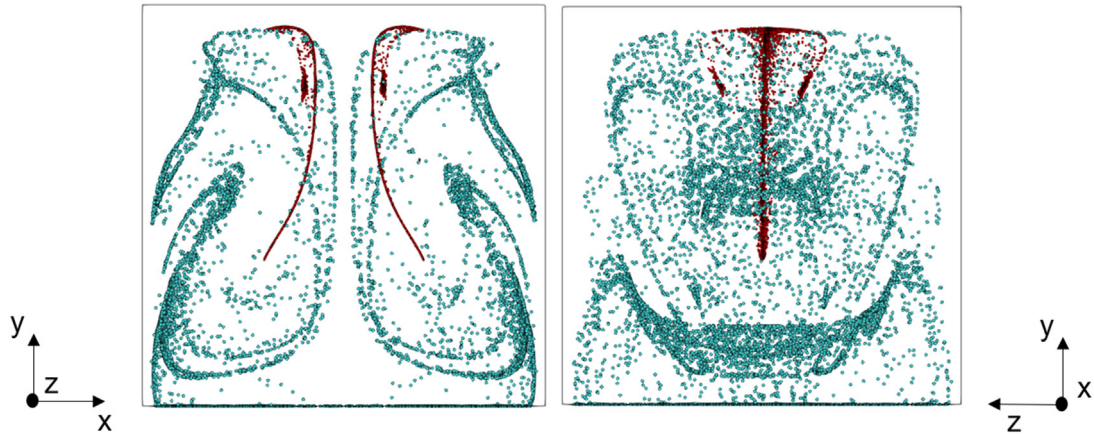


FIG. 24. Superposition of the particle distribution for $\xi = 0.3$ (in green) and $\xi = 1.85$ (in red) for the case of conducting sidewalls and adiabatic front and back walls and $t = 2.364$. Front view (left) and side view (right).

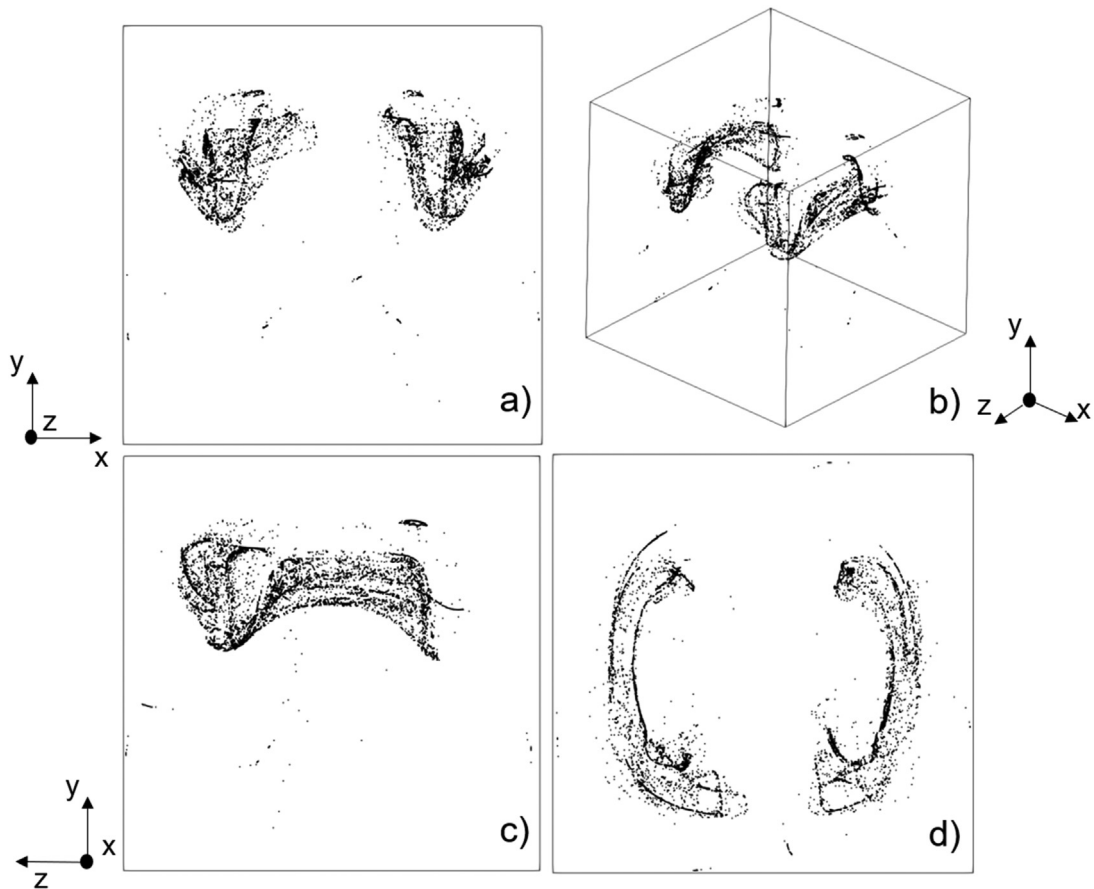


FIG. 25. Particle morphology for the case of fully conducting sidewalls, $\xi = 0.3$ and $t = 2.364$: (a) xy view, (b) 3D view, (c) yz view, (d) xz view.

the illusion of a solid body being shaken inside the liquid.^{27–32} In the present case (parallel vibrations), no asymptotic state exists as the phenomena are intrinsically cyclic and the morphology of the emerging structures is dictated essentially by the thermal boundary conditions

implemented along the sidewalls of the cavity. In place of the “quadrics” structures typical of the perpendicular case, mushroom-like formations or more involved realizations are obtained. In both cases, particle accumulation is enabled by virtue of the compressible nature

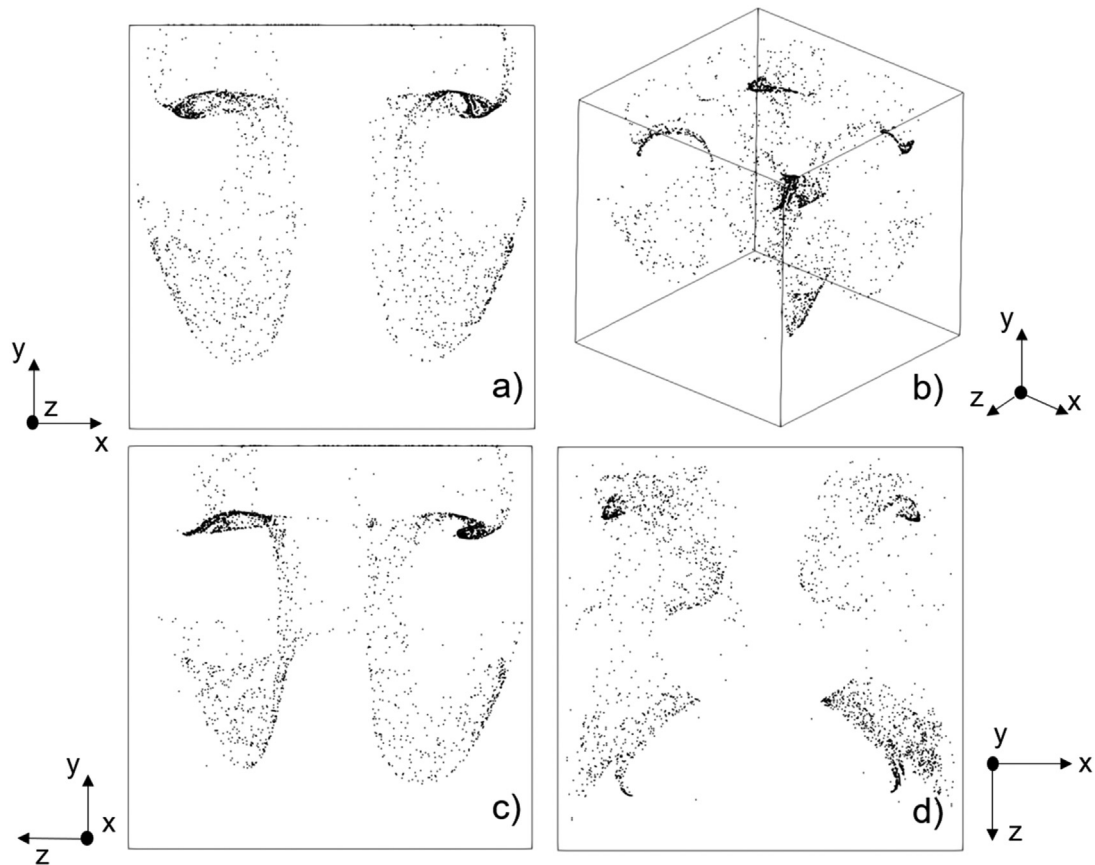


FIG. 26. Particle morphology for the case of fully conducting sidewalls, $\zeta = 1.85$ and $t = 2.364$: (a) xy view, (b) 3D view, (c) yz view, (d) xz view.

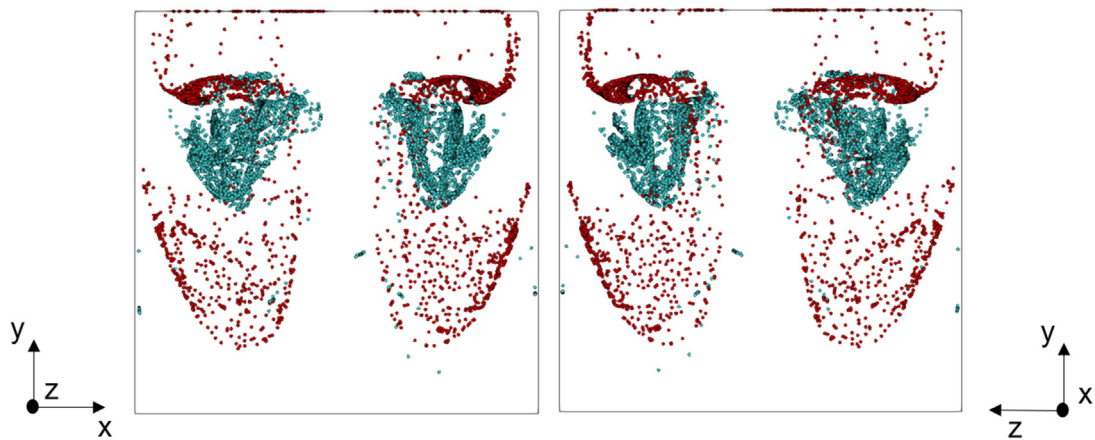


FIG. 27. Superposition of the particle distribution for $\zeta = 0.3$ (in green) and $\zeta = 1.85$ (in red) for the case where all walls are conducting and $t = 2.364$. Front view (left) and side view (right).

of the particle velocity field. However, while in the perpendicular case the accumulation of such compressibility effects results in the aforementioned stationary morphologies, in the parallel one it drives the emergence of asymmetries, which grow with time.

In particular, the structures achieved when applying either fully adiabatic or fully conducting walls bare much resemblance to one another, this being especially true when the heavy particles are considered. In these cases, as a result of the above-mentioned ongoing

symmetry-breaking process, a disruptive region can be identified at the top rear of the cavity. However, this process is greatly mitigated in the situation with the hybrid thermal boundary conditions. This boundary condition also allows for appreciably different particle patterning behaviors, by which heavy particles tend to form compact structures at the center of the cavity, whereas light particles display a more dispersed arrangement.

Possible practical uses aside, the present endeavor should be seen as another attempt to explore the physics of multi-phase (fluid-particle) systems evolving far from conditions corresponding to simple steady flow, other relevant examples of this line of inquiry for other types of thermal convection being the works by Refs. 18, 19, 21–26, and 56–58.

An exciting prospect for the future is the extension of the present analysis (the parallel vibrational case) to conditions for which the underlying fluid flow becomes turbulent, thereby bridging the gap with another important theme running in the literature, namely, that related to the dynamics of solid inertial particles in turbulent flow (Refs. 60–63 and references therein).

ACKNOWLEDGMENTS

This work was supported by the UK Space Agency (STFC Grant Nos. ST/S006354/1, ST/W005588/1, ST/W002256/1, and ST/W007185/1) in the framework of the PARTICLE VIBRATION (T-PAOLA) project.

AUTHOR DECLARATIONS

Conflict of Interest

The authors have no conflicts to disclose.

Author Contributions

Georgie Crewdson: Conceptualization (equal); Data curation (equal); Investigation (equal); Methodology (equal); Software (equal); Validation (equal); Visualization (equal); Writing – original draft (equal). **Marcello Lappa:** Conceptualization (equal); Funding acquisition (equal); Investigation (equal); Project administration (equal); Resources (equal); Supervision (equal); Writing – original draft (equal); Writing – review & editing (equal).

DATA AVAILABILITY

The data that support the findings of this study are openly available in Pure, at <https://doi.org/10.15129/ec6c0bec-0cbc-44ea-a9c0-3e345d9ec645>.

REFERENCES

- V. P. Srivastava, “Particle-fluid suspension model of blood flow through stenotic vessels with applications,” *Int. J. Bio-Med. Comput.* **38**(2), 141–154 (1995).
- C. S. R. Rao, “Fluidized-bed combustion technology—A review,” *Combust. Sci. Technol.* **16**(3–6), 215–227 (1977).
- J. Z. Zhao, L. Ratke, and B. Feuerbacher, “Microstructure evolution of immiscible alloys during cooling through the miscibility gap,” *Model. Simul. Mater. Sci. Eng.* **6**, 123–139 (1998).
- X. Deng and N. Chawla, “Modeling the effect of particle clustering on the mechanical behavior of SiC particle reinforced Al matrix composites,” *J. Mater. Sci.* **41**(17), 5731–5734 (2006).
- Z. Knez, M. K. Hrnčič, and M. Škerget, “Particle formation and product formation using supercritical fluids,” *Annu. Rev. Chem. Biomol. Eng.* **6**, 379–407 (2015).
- T. Wang and Z. Xing, “A fluid-particle interaction method for blood flow with special emphasis on red blood cell aggregation,” *Bio-Med. Mater. Eng.* **24**, 2511–2517 (2014).
- M. Lappa, “A theoretical and numerical multiscale framework for the analysis of pattern formation in protein crystal engineering,” *J. Multiscale Comput. Eng.* **9**(2), 149–174 (2011).
- E. Saeedi, S. Abbasi, K. F. Bohringer, and B. A. Parviz, “Molten-alloy driven self-assembly for nano and micro scale system integration,” *Fluid Dyn. Mater. Process.* **2**(4), 221–246 (2006).
- R. Bürger and W. L. Wendland, “Sedimentation and suspension flows: Historical perspective and some recent developments,” *J. Eng. Math.* **41**, 101–116 (2001).
- P. Venema, “The viscous flow of charged particles through a charged cylindrical tube,” *J. Fluid Mech.* **282**, 45–73 (1995).
- J. Nguyen, D. Valter Conca, J. Stein, L. Bovo, C. A. Howard, and I. L. Garcia, “Magnetic control of graphitic microparticles in aqueous solutions,” *Proc. Natl. Acad. Sci.* **116**(7), 2425–2434 (2019).
- S. Michelin, E. Lauga, and D. Bartolo, “Spontaneous autophoretic motion of isotropic particles,” *Phys. Fluids* **25**(6), 061701 (2013).
- M. Balvin, E. Sohn, T. Iracki, G. Drazer, and J. Frechette, “Directional locking and the role of irreversible interactions in deterministic hydrodynamics separations in microfluidic devices,” *Phys. Rev. Lett.* **103**, 078301 (2009).
- J. Herrmann, M. Karweit, and G. Drazer, “Separation of suspended particles in microfluidic systems by directional-locking in periodic fields,” *Phys. Rev. E* **79**, 061404 (2009).
- T. R. Kirkpatrick and J. K. Bhattacherjee, “Driven active matter: Fluctuations and a hydrodynamic instability,” *Phys. Rev. Fluids* **4**, 024306 (2019).
- D. V. Lyubimov, T. P. Lyubimova, and A. V. Straube, “Accumulation of solid particles in convective flows,” *Microgravity Sci. Technol.* **16**(1), 210–214 (2005).
- R. Parker, P. Capobianchi, and M. Lappa, “Competing particle attractee in liquid bridges,” *Philos. Trans. A* **381**(2244), 20220302 (2023).
- A. L. Yarin, T. A. Kowalewski, W. J. Hiller, and S. Koch, “Distribution of particles suspended in convective flow in differentially heated cavity,” *Phys. Fluids* **8**, 1130 (1996).
- J. Kalilainen, P. Rantanen, T. Lind, A. Auvinen, and A. Dehbi, “Experimental investigation of a turbulent particle-laden flow inside a cubical differentially heated cavity,” *J. Aerosol Sci.* **100**, 73–87 (2016).
- M. A. Sayed, A. Dehbi, M. Hadziabić, B. Ničeno, and K. Mikityuk, “CFD simulation of particle-laden flow in a 3D differentially heated cavity using coarse large eddy simulation,” *Flow Turbul. Combust.* **109**, 961–990 (2022).
- T. H. Solomon and J. P. Gollub, “Passive transport in steady Rayleigh–Bénard convection,” *Phys. Fluids* **31**(6), 1372–1372 (1988).
- T. H. Solomon and J. P. Gollub, “Chaotic particle transport in time-dependent Rayleigh–Bénard convection,” *Phys. Rev. A* **38**(12), 6280 (1988).
- H. J. Park, K. O’Keefe, and D. H. Richter, “Rayleigh–Bénard turbulence modified by two-way coupled inertial, nonisothermal particles,” *Phys. Rev. Fluids* **3**(3), 1–15 (2018).
- L. Jiang, E. Calzavarini, and C. Sun, “Rotation of anisotropic particles in Rayleigh–Bénard turbulence,” *J. Fluid Mech.* **901**, A8 (2020).
- A. Xu, S. Tao, L. Shi, and H. D. Xi, “Transport and deposition of dilute microparticles in turbulent thermal convection,” *Phys. Fluids* **32**, 083301 (2020).
- W. Yang, Y. Z. Zhang, B. F. Wang, Y. Dong, and Q. Zhou, “Dynamic coupling between carrier and dispersed phases in Rayleigh–Bénard convection laden with inertial isothermal particles,” *J. Fluid Mech.* **930**, A24 (2022).
- M. Lappa, “The patterning behavior and accumulation of spherical particles in a vibrated non-isothermal liquid,” *Phys. Fluids* **26**(9), 093301 (2014).
- M. Lappa, “Numerical study into the morphology and formation mechanisms of three-dimensional particle structures in vibrated cylindrical cavities with various heating conditions,” *Phys. Rev. Fluids* **1**(6), 064203 (2016).
- M. Lappa, “On the nature, formation and diversity of particulate coherent structures in microgravity conditions and their relevance to materials science and problems of astrophysical interest,” *Geophys. Astrophys. Fluid Dyn.* **110**(4), 348–386 (2016).

- ³⁰M. Lappa, “On the multiplicity and symmetry of particle attractors in confined non-isothermal fluids subjected to inclined vibrations,” *Int. J. Multiphase Flow* **93**, 71–83 (2017).
- ³¹M. Lappa, “Characterization of two-way coupled thermovibrationally driven particle attractee,” *Phys. Fluids* **34**(5), 053109 (2022).
- ³²M. Lappa and T. Burel, “Symmetry breaking phenomena in thermovibrationally driven particle accumulation structures,” *Phys. Fluids* **32**(5), 053314 (2020).
- ³³G. Crewdson and M. Lappa, “An investigation into the behavior of non-isodense particles in chaotic thermovibrational flow,” *Fluid Dyn. Mater. Process.* **18**(3), 497–510 (2022).
- ³⁴G. Crewdson, M. Evans, and M. Lappa, “Two-dimensional vibrationally-driven solid particle structures in non-uniformly heated fluid containers,” *Chaos* **32**(10), 103119 (2022).
- ³⁵D. Haller and T. Sapsis, “Where do inertial particles go in fluid flows?,” *Physica D* **237**(5), 573–583 (2008).
- ³⁶T. Sapsis and G. Haller, “Clustering criterion for inertial particles in two-dimensional time-periodic and three-dimensional steady flows,” *Chaos* **20**, 017515 (2010).
- ³⁷S. S. Tabakova and Z. D. Zapruanov “On the hydrodynamic interaction of two spheres oscillating in a viscous fluid. I. Axisymmetrical case,” *J. Appl. Math. Phys.* **33**, 344–357 (1982); “On the hydrodynamic interaction of two spheres oscillating in a viscous fluid. II. Three dimensional case,” **33**, 487–502 (1982).
- ³⁸R. Wunenburger, V. Carrier, and Y. Garrabos, “Periodic order induced by horizontal vibrations in a two-dimensional assembly of heavy beads in water,” *Phys. Fluids* **14**(7), 2350–2359 (2002).
- ³⁹A. A. Ivanova, V. G. Kozlov, and A. F. Kuzaev, “Vibrational lift force acting on a body in a fluid near a solid surface,” *Dokl. Phys.* **50**(6), 311–314 (2005).
- ⁴⁰V. G. Kozlov, A. A. Ivanova, and P. Evesque, “Block stratification of sedimenting granular matter in a vessel due to vertical vibration,” *Fluid Dyn. Mater. Process.* **2**(3), 203–210 (2006).
- ⁴¹G. Crewdson and M. Lappa, “Spatial and temporal evolution of three-dimensional thermovibrational convection in a cubic cavity with various thermal boundary conditions,” *Phys. Fluids* **34**(1), 014108 (2022).
- ⁴²T. Lyubimova and K. Kovalevskaya, “Gravity modulation effect on the onset of thermal buoyancy convection in a horizontal layer of the Oldroyd fluid,” *Fluid Dyn. Res.* **48**, 061419 (2016).
- ⁴³G. Crewdson and M. Lappa, “The zoo of modes of convection in liquids vibrated along the direction of the temperature gradient,” *Fluids* **6**(1), 30 (2021).
- ⁴⁴M. R. Maxey and J. J. Riley, “Equation of motion for a small rigid sphere in a nonuniform flow,” *Phys. Fluids* **26**, 883–889 (1983).
- ⁴⁵M. Lappa, “On the variety of particle accumulation structures under the effect of g-jitters,” *J. Fluid Mech.* **726**, 160 (2013).
- ⁴⁶P. Capobianchi and M. Lappa, “On the influence of gravity on particle accumulation structures in high aspect-ratio liquid bridges,” *J. Fluid Mech.* **908**, A29 (2021).
- ⁴⁷M. Lappa, “Incompressible flows and the Boussinesq approximation: 50 years of CFD,” *C.R. Méc.* **350**(S1), 22 (2022).
- ⁴⁸P. M. Gresho, “Incompressible fluid dynamics: Some fundamental formulation issues,” *Annu. Rev. Fluid Mech.* **23**, 413–453 (1991).
- ⁴⁹O. A. Ladyzhenskaya, *The Mathematical Theory of Viscous Incompressible Flow*, 2nd ed. (Gordon and Breach, New York, NY; London, UK, 1969).
- ⁵⁰H. Helmholtz, “On Integrals of the hydrodynamical equations, which express vortex-motion,” *London Edinburgh Dublin Philosoph. Magaz. J. Sci.* **33**(226), 485–512 (1867).
- ⁵¹J.-L. Guermond, “Some practical implementations of projection methods for Navier–Stokes equations,” *Model. Math. Anal. Numer.* **30**, 637–667 (1996).
- ⁵²J.-L. Guermond and L. Quartapelle, “On stability and convergence of projection methods based on pressure Poisson equation,” *Int. J. Numer. Methods Fluids* **26**, 1039–1053 (1998).
- ⁵³J.-L. Guermond, P. Mineev, and J. Shen, “An overview of projection methods for incompressible flows,” *Comput. Methods Appl. Mech. Eng.* **195**, 6011–6045 (2006).
- ⁵⁴J. C. Strikwerda and Y. S. Lee, “The accuracy of the fractional step method,” *SIAM J. Numer. Anal.* **37**, 37–47 (1999).
- ⁵⁵N. A. Petersson, “Stability of pressure boundary conditions for Stokes and Navier–Stokes equations,” *J. Comput. Phys.* **172**, 40–70 (2001).
- ⁵⁶D. E. Melnikov and V. Shevtsova, “Different types of Lagrangian coherent structures formed by solid particles in three-dimensional time-periodic flows,” *Eur. Phys. J. Spec. Top.* **226**, 1239 (2017).
- ⁵⁷M. Gotoda, A. Toyama, M. Ishimura, T. Sano, M. Suzuki, T. Kaneko, and I. Ueno, “Experimental study of coherent structures of finite-size particles in thermocapillary liquid bridges,” *Phys. Rev. Fluids* **4**, 094301 (2019).
- ⁵⁸T. Sakata, S. Terasaki, H. Saito, S. Fujimoto, I. Ueno, T. Yano, K. Nishino, Y. Kamotani, and S. Matsumoto, “Coherent structures of $m = 1$ by low-Stokes number particles suspended in a half-zone liquid bridge of high aspect ratio: Microgravity and terrestrial experiments,” *Phys. Rev. Fluids* **7**, 014005 (2022).
- ⁵⁹M. Lappa, “On the transport, segregation and dispersion of heavy and light particles interacting with rising thermal plumes,” *Phys. Fluids* **30**(3), 033302 (2018).
- ⁶⁰S. Elghobashi and G. C. Truesdell, “Direct simulation of particle dispersion in a decaying isotropic turbulence,” *J. Fluid Mech.* **242**, 655–700 (1992).
- ⁶¹L.-P. Wang and M. R. Maxey, “Settling velocity and concentration distribution of heavy particles in homogeneous isotropic turbulence,” *J. Fluid Mech.* **256**, 27–68 (1993).
- ⁶²T. Fallon and C. B. Rogers, “Turbulence-induced preferential concentration of solid particles in microgravity conditions,” *Exp. Fluids* **33**(2), 233–241 (2002).
- ⁶³K. Matsuda, K. Schneider, and K. Yoshimatsu, “Scale-dependent statistics of inertial particle distribution in high Reynolds number turbulence,” *Phys. Rev. Fluids* **6**, 064304 (2021).